Pharmacokinetics and Dosimetry of Gallium-68 labelled Sarabesin 3 for Prostate Cancer

Master thesis

J.J.M. Kouwenberg

In partial fulfilment of the requirements for the degree of

Master of Science
in Biomedical Engineering

at the Delft University of Technology and Erasmus Medical Center.

Professor:	Prof. dr. ir. F. Beekman
Supervisor TU Delft:	Dr. ir. A.G. Denkova
Supervisor Erasmus MC:	Ir. M. Segbers
	Dr. M. Konijnenberg

Date of Submission:	16-06-2015
Date of Presentation:	23-06-2015

Erasmus MC
University Medical Center Rotterdam

TU Delft
Delft University of Technology

A complex system that works is invariably found to have evolved from a simple system that works.

John Gaule
English Puritan cleric, 1603-1687

Abstract

Objective: Prostate cancer remains one of the most prevalent forms of cancer in men aged over 65 years, with yearly around 11,200 new cases and 2,600 deaths in the Netherlands. Diagnosis of prostate cancer still relies on biopsies, which are unpleasant and invasive procedures for the patient. The new PET tracer, [^{68}Ga]Sarabesin 3, aims to offer an accurate and minimally invasive way to locate and diagnose PC by taking benefit of the overexpression of the gastrin releasing peptide receptor on prostate cancer cells. In this research, the pharmacokinetics of the tracer in cancerous and healthy tissues from dynamic PET imaging was studied to identify receptor-specific uptake in prostate cancer tissue.

Methods: An image derived input function was obtained from a volume of interest drawn over the femoral artery. The image derived input function correction methods proposed by Chen[1], Mourik[2] and Hackett[3] were evaulated using Monte Carlo simulation of the fermoral artery. The simulation was done in GATE using a model of the Siemens Biograph mCT. Iteratively reweighted least squares and step-wise model fitting were used to increase the accuracy in the small spots suspicious of cancerous tissue. In order to validate the applied arterial input function correction methods, a model of the Siemens Biograph mCT was built in the GATE Monte Carlo software. The absorbed dose was calculated using the MIRD male dosimetry model, OLINDA/EXM and the time activity curves in the various organs. A simple one-way perfusion model of the kidney was applied to estimate the bladder filling over time.

Results: The sensitivity and spatial resolution of the GATE model at the field-of-view center were respectively 11,1 ± 0,027 kcps/MBq and 4,00 ± 0,56 mm full width half maximum in the radial direction, both closely matching the values of reported by Jakoby[4]. Applying the arterial input function correction methods to the simulated arterial and venous concentration curves showed that Hackett's method[3] most accurately estimates the true arterial concentration with less than 1% error after the first pass peak. Step-wise fitting of the 1-, FDG- and 2-compartment models showed to be less vulnerable to local minima. An increase up to 280% receptor density was observed in the spots suspicious of cancerous tissue compared to the surrounding tissue healthy prostate tissue, thereby providing proof for the specific uptake of [^{68}Ga]Sarabesin 3 by gastrin releasing peptide receptor in prostate cancer tissue. The pharmacokinetics of [^{68}Ga]Sarabesin 3 were best described by a FDG model or a 2 compartment model with a small retention coefficient. It was not possible to determine the retention coefficient of the latter due the relatively large noise and small number of measurement points 50 minutes post-injection.

Conclusion: Hackett's method estimated the arterial concentration well in Monte Carlo simulations. [^{68}Ga]Sarabesin 3 showed a good uptake in spots suspicious of cancerous tissue and had a high retention despite being an antagonist. The absorbed dose per administered activity to the prostate, red bone marrow and pancreas were estimated at 16,5, 13,5 and 196 μGy/MBq and the effective dose was 22,40 μSv/MBq, which is similar to the average [^{18}F]DG effective dose.

Abbreviations

AIF	Arterial Input Function
cAIC	corrected Akaike Information Criteria
BIC	Bayesian Information Criteria
FBP	Filtered Back Projection
FDG	Fluorodeoxyglucose
FOV	Field Of View
FWHM	Full Width Half Maximum
GRPr	Gastrin Releasing Peptide receptor
IDIF	Image Derived Input Function
IRLS	Iteratively Reweighted Least Squares
LOR	Line Of Response
LSO	Lutetium Orthosilicate
MSRB	Multi Slice Rebinning
PC	Prostate Cancer
PET	Positron Emission Tomography
PVE	Partial Volume Effects
TAC	Time Activity Curve
TTC	Time Tracer Curve
VOI	Volume Of Interest

Contents

Introduction

While Prostate Cancer (PC) remains one of the most prevalent forms of cancer in older men, diagnosis in the form of biopsies is often still invasive and unpleasant for the patient. This thesis focused on the novel PC tracer [^{68}Ga]Sarabesin 3. This tracer has a high affinity for the Gastrin Releasing Peptide receptor (GRPr), which is overexpressed in PC, but is also found in healthy prostate, pancreatic and other tissues[5]. The pharmacokinetic properties and dosimetry of this novel tracer were studied in healthy and PC tissue. A number of difficulties had to be overcome in order to obtain reliable models of the behaviour of the tracer, including an Image Derived Input Function (IDIF), small spots suffering from significant Partial Volume Effects (PVE) and a limited number of measurement points. Since an error in the IDIF propagates throughout the whole pharmacokinetic fitting process, extra effort was made to validate the used IDIF correction methods using Monte Carlo simulation. A model of the Siemens Biograph mCT was made in GATE to approximate the Siemens Biograph mCT PET scanner for these simulations. Monte Carlo simulations were used instead of phantom scans since the former allows for very precise control of the input parameters. Finally, since the tracer was coupled to an isotope, it was important to estimate the risk introduced by the radiation. Using the earlier obtained pharmacokinetic model and activity over time curves in the critical organs, an approximation of the absorbed dose in said organs could be made.

This thesis was performed as part of the master Biomedical Engineering specialization Medical Physics at Delft University of Technology in collaboration with Erasmus Medical Center.

This thesis was preceded by a literature review with a more extensive background on the subjects of this thesis.

Materials and Methods

1. *[^{68}Ga]Sarabesin 3 and Clinical Procedure*

In the scope of a larger study investigating the [^{68}Ga]Sarabesin 3's ability to visual prostate tumours, led by I. Bakker, male patients between 40 and 70 years old with a primary tumour confined to the prostate and no known metastases were asked to participate[6]. Those who agreed underwent the Sarabesin 3 scan procedure in addition to their regular treatment, which included a radical prostatectomy. Each patient was injected with 40 µg Sarabesin 3 labelled with 150 to 200 MBq Gallium 68, resulting in approximately 0,01% labelled tracer or 6 to 8 MBq/nmol, in a 1 minute during bolus. The dynamic scan was initiated at the start of the injection. After injection of the tracer, the patient was submitted to a number of PET/CT scans, venous and urine samples for a period of approximately 4 hours. Slices of the prostate, removed during the radical prostatectomy, were marked by a pathologist and an autoradiography was made to visualize the receptor expression. The pelvic area was scanned at 0-30 (dynamic), 30, 45, 60 (whole body), 115 (whole body), 150 and 210 minutes post-injection for respectively 30, 6, 6, 25, 30, 12 and 12 minutes. Venous samples were taken from the right ulnar vein at 5, 10, 20, 30, 45, 60, 100, 140 and 180 minutes and their activity was measured using a gamma counter. A urinary catheter was inserted and the urine collector was replaced at 30, 60, 90 and 180 minutes after which the activity in each collector was measured.

2. *Pharmacokinetic Modeling*

2.1. Quantitative PET Measurement

All scans were made using a Siemens Biograph mCT calibrated using the EANM guidelines[7]. Reconstruction was done via iterative reconstruction with Time-of-Flight, a 3 mm Point Spread Function (PSF) and Gaussian smoothing filter. The organs of interest and the femoral vein and artery, the latter two over a length of approximately 2 cm, were delineated on the CT scan corresponding to the respective PET scan using PMod as shown in Figure 1. Spots assessed by an experienced nuclear medicine physician as suspicious for tumour tissue were measured by their SUV_{peak} value, defined as a 1 cm diameter sphere around the hottest pixel.

The measured activity was corrected for decay to the time of injection and the time points were defined at the mid frame interval. The tracer concentration was calculated by multiplying the decay corrected activity by the tracer activity at the time of injection in pmol/MBq.

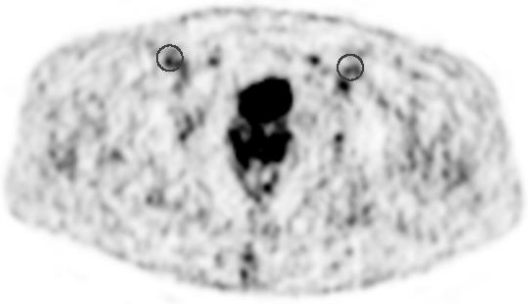

Figure 1: *The femoral arteries marked in a reconstruction of the pelvic area*

2.2. Arterial Input Function

Since direct arterial sampling was not possible, an IDIF approach was used. Chen's[1], Hackett's[3] and Mourik's[2] PVE correction methods were evaluated. These methods with their

respective ROIs are given in the Literature Review. The resulting corrected Arterial Input Function (AIF) was fitted to a tri-exponential given in equation 1 [3] to reduce the noise contribution using non-weighted least-squares fitting[8].

$$c_a(t) = D_0[(A_1 \cdot t - A_2 - A_3) \cdot e^{-L_1 t} + A_2 \cdot e^{-L_2 t} + A_3 \cdot e^{-L_3 t}] \quad 1$$

Calculation of the corrected AIF and tri-exponential were done with software written specifically for this thesis. All in-house written software was written using MATLAB 2014a and MathWorks' Optimization Toolbox[1].

2.3. Pharmacokinetic Modeling

The 1-, FDG- and 2 Compartment models and Patlak and Logan plots[9] were evaluated for each Volume of Interest (VOI) based on visual inspection, the corrected Akaike Information Criteria (cAIC) and the Bayesion Information Criteria (BIC). The slope parameters from the Patlak and Logan plots were compared to the respective slope parameters calculated using the compartment model fits[10]. A brief introduction into the various models and linearizations are given in APPENDIX A : Compartment models and Linearizations. Weighted least-squares fitting of the models was done using in-house written software written which allowed for fitting using either an analytical or an Runge-Kutta Ordinary Differential Equation (ODE) solution. The analytical solution, given in given in APPENDIX B : ANALYTICAL SOLUTION 2 COMPARTMENT MODEL, was calculated using MathWorks' Symbolic Toolbox. Fitting of the models was done using robust IRLS[11] using Mathworks' Statistics Toolbox and the default settings, which returned the estimated value and confidence interval for each parameter. Since the exact AIF error was unknown and expected to be low, it was assumed that the error in the AIF was negligible compared to the error in the fitting parameters during the calculations, despite the possible bias error in the fitting parameters [12]. The calculated k_3 parameters, a value directly proportional to the receptor density[9], were compared to their respective regions in the autoradiography and pathological report in order to compare the results.

Due to the relatively large noise and PVE contribution in the small SUV_{peak} spot VOIs, the following variance reducing procedure, partly based on Millet's work[13], was applied. First a 1 Compartment fit was done on the whole prostate to calculate the blood time delay, τ , in the organ and the average blood volume in the prostate, followed by a 2 Compartment fit on the same region with the known blood time delay and blood volume to calculate the disassociation constant, k_4. This constant is independent of the receptor density and therefore the same in healthy prostate and tumour tissue. Thirdly, a 2 compartment and a FDG model with the precalculated parameters were fitted to obtain the respective k_3 parameters. This variance reducing procedure was then compared to a direct fit of the respective compartment models.

2.4. Metabolite correction

50% alcohol solution was added to venous samples immediately after extraction to halt the metabolic reactions. The intact compound fraction in the samples was measured using High-Performance Liquid Chromatography (HPLC) by the technicians.

[1] © 2015 The MathWorks, Inc. MATLAB and Simulink are registered trademarks of The MathWorks, Inc.

3. MIRD Dosimetry

The organ specific and effective doses were estimated by calculating the total amount of disintegrations per organ and applying these values to the MIRD dosimetry model of an adult male using OLINDA/MEX[14]–[16]. The Time Tracer Curves (TTCs), or tracer concentration over time, of the liver, kidneys and spleen were estimated by fitting a 1 Compartment model while a FDG model was used for the pancreas. The prostate TTC was taken from the pharmacokinetic analysis. A kidney-to-urine perfusion factor was estimated using the following equation:

$$P = \sum_i A'_{samples,i} \Big/ \int_{t_0}^{t_1} A'_{kidneys}(t) \qquad 2$$

Where P is the perfusion factor, $A'_{samples,i}$ is the total decay corrected activity in sample i and $A'_{kidneys}$ is the total decay corrected activity in the kidneys. The bladder filling curve then followed from multiplying the activity in the kidneys with the perfusion factor. The TTC in the red bone marrow was calculated as 1500 grams of blood and a 1:1 blood-red bone marrow concentration ratio was assumed[17]. All TTCs were converted to Time Activity Curves (TACs) similar to the inverse procedure given in section 2.1 and integrated to obtain the total number of disintegrations given as MBq-h/MBq.

4. Monte Carlo PET Simulation

In order to validate the used correction methods for the AIF, a Monte Carlo simulation of the Siemens Biograph mCT was done using GATE v7.0[18], [19]. Since the Monte Carlo method was not elaborated in the literature review, a brief introduction is given in APPENDIX C : Monte Carlo Method and GATE. All simulations were executed on the European Grid Infrastructure (EGI) using GateLab[20].

4.1. Geometry[4], [21]

The Siemens Biograph mCT was modelled as a cylindricalPET with an inner radius of 42,45 cm and length of 21,65 cm in the axial direction. The scanner consists of 48 evenly spaced 25 mm x 54 mm x 216,5 mm (radial x transaxial x axial) detector heads. In order to approximate the scattering well, two lead ring shields at the ends of the detector were added. Each detector head was filled with 4 detector blocks evenly spaced in the axial direction, where each respective detector block contains 48 x 48 detector. The dimension of a detector block and a detector are respectively 25 mm x 54 mm x 54 mm and 25 mm x 4 mm x 4 mm, with the latter having a spacing of 0,18 mm. The model was simplified by decreasing the spacing between the detector blocks in the axial direction to match the detector spacing, thereby removing the need for pseudo rings during

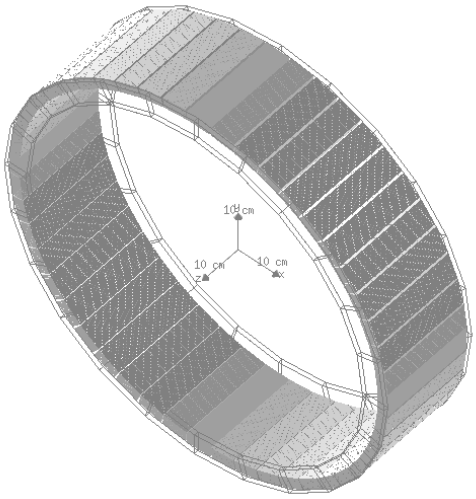

Figure 2: *Siemens Biograph mCT model rendered in GATE v7.0*

reconstruction. Each detector was simulated as a combination of 20 mm LSO and 5 MM plastic, the latter representing the casing and electronics. A ^{176}Lu source with 330 Bq/mL LSO was added to simulate the natural activity of LSO. A render of the resulting model is shown in Figure 2.

4.2. Digitizer[4], [21]

The electronics and data processing were simulated using digitizer components in GATE. First an adder was added which integrates all the detected energy and locates the origin of the event in the detector block. This was followed by some energy blurring, which blurred the detected energy with a resolution of 11,7% and a reference energy of 511 keV. The time is discretized to 527 ps intervals and each detector block experienced a 60 ns paralyzable dead-time. The final stage was an energy thresholder which only allowed events between 435 and 650 keV, after which an event was marked as a single. The resulting singles were used to construct coincidence events using a coincidence window of 4,1 ns. A delay window of an arbitrarily chosen value of 500 ns was added for random correction.

4.3. Phantoms and sources

The phantom in each simulation was an approximation of the upper leg given by a 20 cm long 10 cm radius cylinder filled with water. The calibration source was a sphere with a radius of 5 cm and an initial activity of 2 MBq, similar to the maximum activity in the simulated arterial input functions, located in the center of the cylinder. The half-life was 2000 s and chosen as to collect a sufficient amount of counts per activity level. The spatial resolution was determined in accordance to the NEMA UN 2-2007 protocol using four 0,55 mm diameter spheres filled with 10 MBq non-decaying activity placed at respectively 1 cm axial, 1 cm radial, 10 cm radial and 10 cm transaxial from the center. The femoral vein and artery were modelled as two 2 cm long cylinders located at the center with a radius of 5 mm with 1 mm spacing, as shown in Figure 3. The artery and vein phantoms were filled with TACs given in Results section 2.2.1.

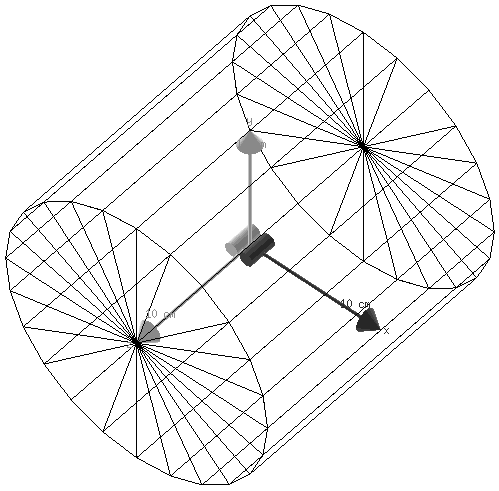

Figure 3: Thigh phantom with artery (black) and vein (grey)

4.4. Reconstruction and calibration

The output from GATE was given in the ROOT format, which contains all the (delayed) coincidence events and their respective energy, location, origin and time. The trues, scatters, randoms and scatter fraction for the calibration source were calculated using the ROOT output. The sensitivity was given by[19]:

$$Sensitivity = {}^{T}/_{A_{FOV}} \quad 3$$

Where T is the trues count rate in kcps and A_{FOV} is the activity in the Field of View (FOV) in MBq. The scatter fraction was calculated using[19]:

$$SF = {}^{S}/_{S+T} \quad (4)$$

Where SF is the dimensionless scatter fraction and S is the scatter count rate in kcps. For reconstruction, all coincidence events were converted to lines of responses (LORs) using the locations of the respective LSO crystals from the model. Random coincidences acquired from the delay window were subtracted from the LORs before conversion of the LORs to sinograms[22]. Construction of the sinograms was performed using Multi Slice Rebinning (MSRB) with a span of 1 and a maximum ring difference of 52 using a script by Sadek A. Nehmeh and CR Schmidtlein which was modified to allow for random correction and dynamic scan reconstruction for this thesis. Arc correction was applied to the sinograms and the resulting corrected sinograms were constructed via Filtered Back Projection (FBP) and a 3 mm Gaussian kernel, all using the STIR library.

The calibration source was simulated for six half-lifes after which eight 1500 s time frames were reconstructed. A 1 cm spherical VOI was placed in the center of the source to measure the non-calibrated activity concentration after which the calibration factor could be calculated. It was assumed that the geometrical correction factor was constant close to the center. The calculated calibration factor was therefore a combination of the geometrical and activity calibration factor. The spatial resolution estimation sources were simulated for 300 s after which Gaussian distributions were fitted to the source points to measure the Full Width Half Maximum (FWHM) in the axial, transaxial and radial direction using MATLAB 2014a.

4.5. AIF Validation

Ten arterial and venous TACs were generated by random sampling from a Gaussian distribution of the tri-exponential coefficients obtained from applying Chen's approach to the second patient. The generated TACs were constructed so that the venous and arterial concentrations matched 60 minutes post-injection and were multiplied by a factor 1 to allow for accurate FBP reconstruction. The simulated scan times and durations matched those of the clinical procedure. Simulated venous samples were calculated from the arterial concentration to prevent bias from a possible mismatch between the generated arterial and venous concentration. The earlier mentioned PVE correction methods were evaluated based on the errors over time:

$$\%Error\ (t) = \left[{}^{AIF_{calculated}\ (t) - TAC_{art}\ (t)}/_{TAC_{art}\ (t)} \right] \cdot 100\% \quad (5)$$

Where $AIF_{calculated}$ is the calculated AIF using one of the correction methods and TAC_{art} is the corresponding true activity concentration.

Results

1. Pharmacokinetic Modeling

A total of three patients participated at the moment of writing. However, the first patient and third patient studies experienced issues leaving only the second patient study available for pharmacokinetic analysis.

1.1. PET Volumes of Interest

Figure 4 (left) shows the whole body PET scan at 60 minutes of the second patient. Figure 4 (right) is a reconstruction of the pelvic area with both spots suspicious of cancerous tissue marked. The pancreas and bladder are clearly in the whole body scan. The anterior spot in the prostate was not analyzed due to interference by the hot bladder.

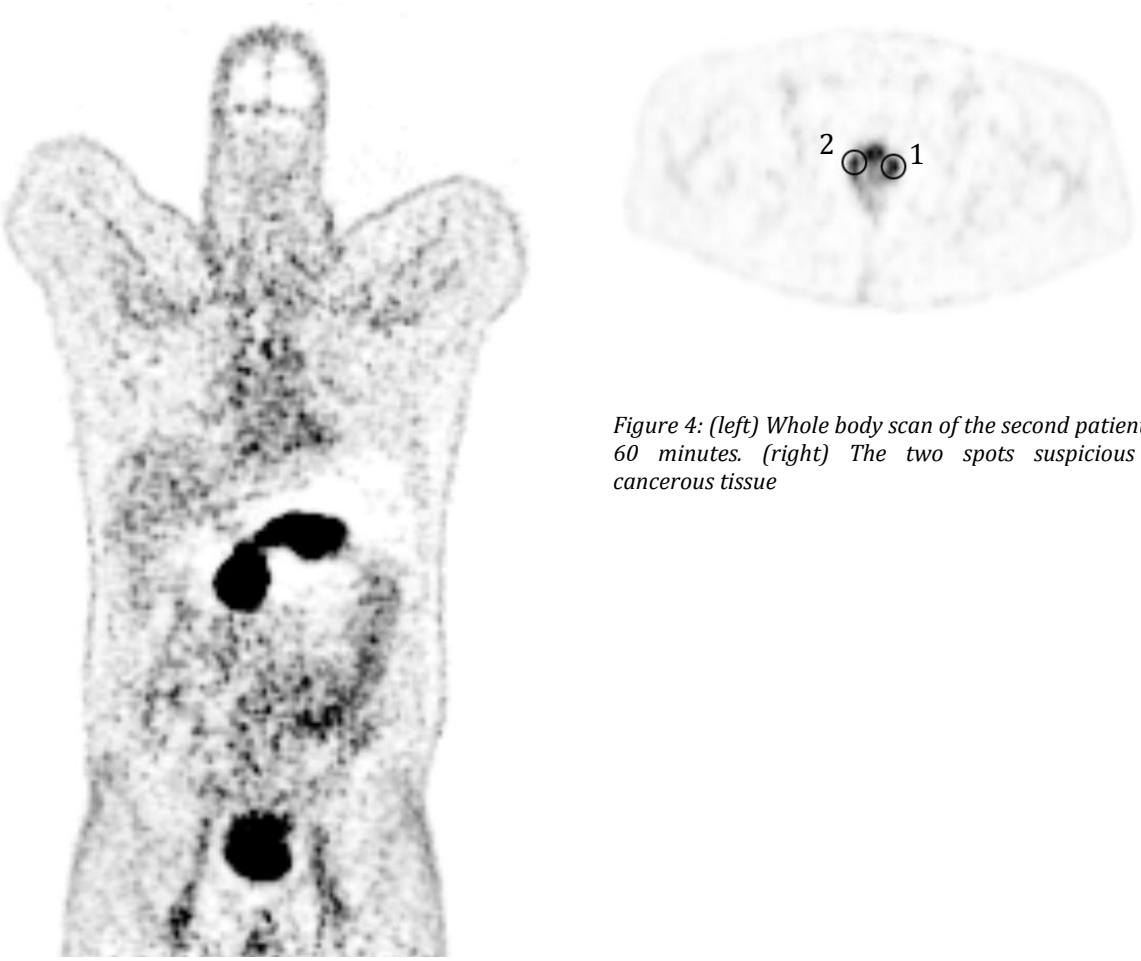

Figure 4: (left) Whole body scan of the second patient at 60 minutes. (right) The two spots suspicious of cancerous tissue

1.2. Arterial Input Function

The AIF for the second patient, derived using Hackett's method, which performed best as shown in Result section 2.2, is shown in Figure 5. The respective tri-exponential parameters are given in Table 1. No metabolization of the tracer was observed in the samples taken during the procedure.

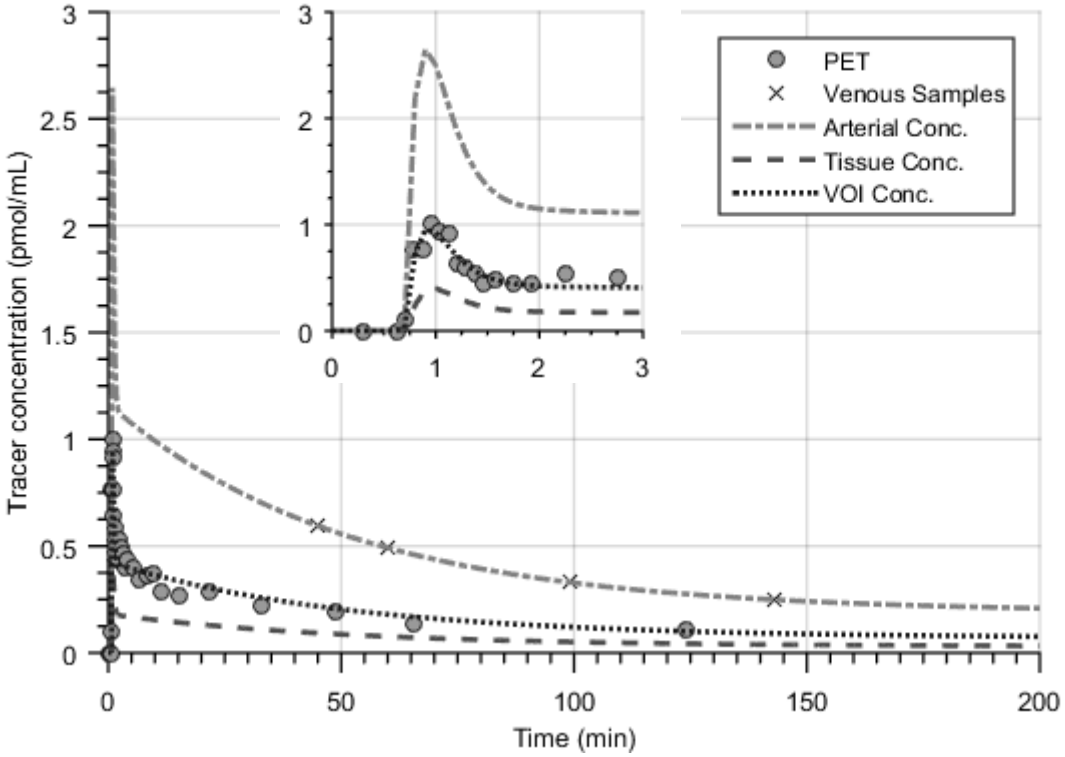

Figure 5: Patient AIF derived using Hackett's method

Table 1: Patient AIF tri-exponential parameters

A_1 (kBq/mL)	A_2 (kBq/mL)	A_3 (kBq/mL)	L_1 (min^{-1})	L_2 (min^{-1})	L_3 (min^{-1})	τ (min)
29,39	0,963	0,189	5,75	0,020	3,62E-14	0,696

1.3. 1 Compartment Model

Figure 6 displays the 1 compartment fits for the three VOIs while Table 2 contains the corresponding fit parameters and information criteria. The grey area is an approximation of the 95% confidence interval of the fit. The size of the measurement points is proportional to their weight factors returned by the IRLS procedure.

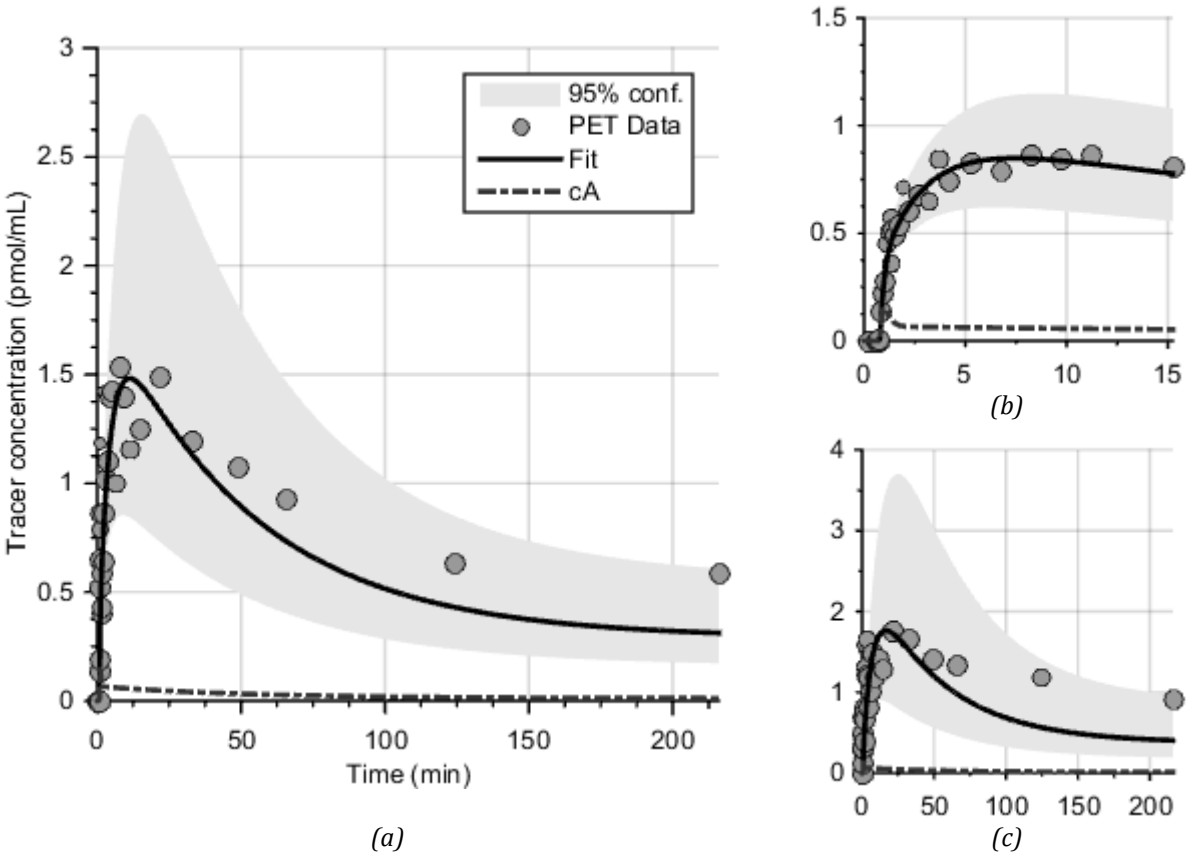

Figure 6: 1 Compartment fit of the first spot (a), the whole prostate (b) and the second spot (c)

Table 2: 1 Compartment fit parameters

1 Compartment	***V_a (%)***	***τ (min)***	***K_1 (min^{-1})***	***k_2 (min^{-1})***
Prostate	5,78 ± 52%	0,78 ± 6%	0,37 ± 15%	0,45 ± 19%
Spot 1	*5,78*	*0,78*	0,41 ± 27%	0,26 ± 36%
- direct	8,87 ± 126%	0,68 ± 31%	0,39 ± 33%	0,25 ± 46%
Spot 2	*5,78*	*0,78*	0,31 ± 32%	0,15 ± 45%
- direct	8,16 ± 158%	0,60 ± 55%	0,27 ± 33%	0,12 ± 51%
	#parameters	**cAIC**	**BIC**	**MSE**
Prostate	4	-147,34	-142,96	0,0074
Spot 1	4	-77,72	-73,34	0,0655
Spot 2	4	-56,21	-51,83	0,1283

**cursive values were obtained from the whole prostate fit*

1.4. FDG Model

Figure 7 displays the FDG model fits for the three VOIs while Table 3 contains the corresponding fit parameters and information criteria.

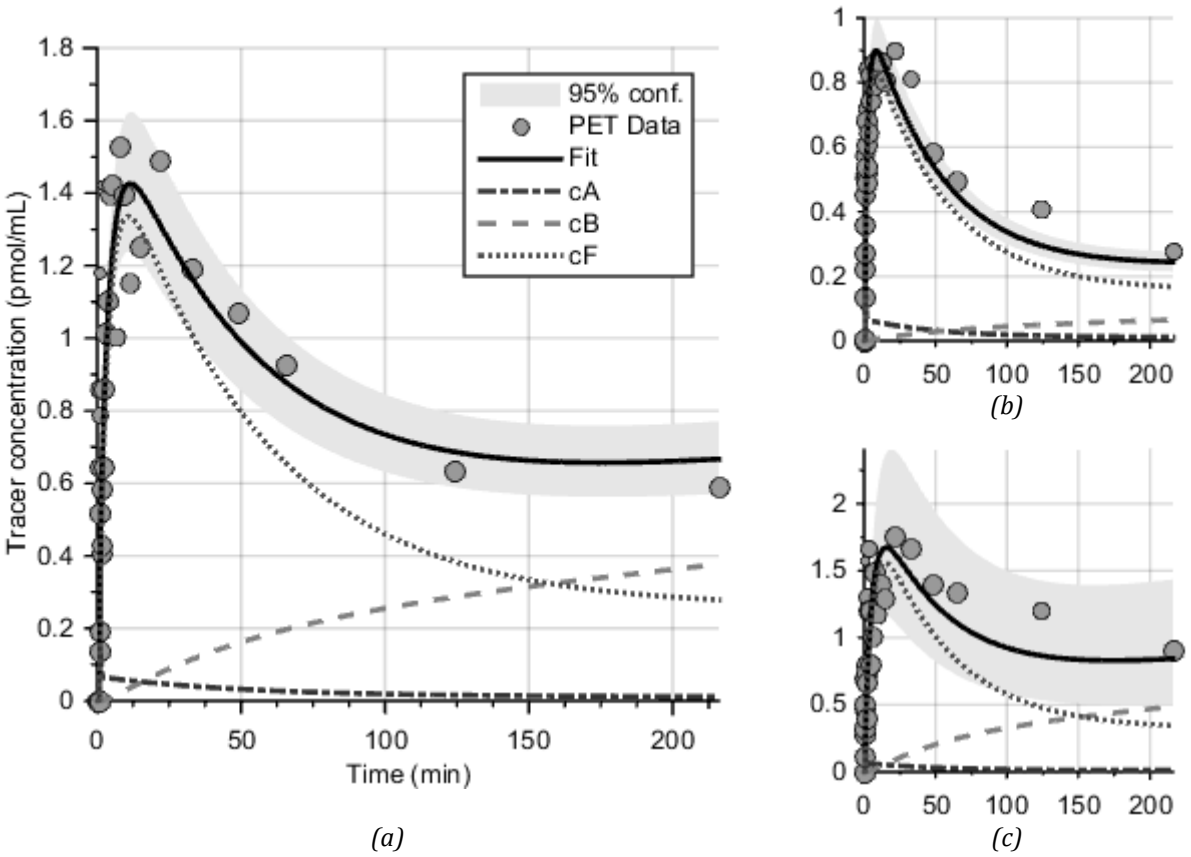

Figure 7: FDG Model fit of the first spot (a), the whole prostate (b) and the second spot (c)

Table 3: FDG Model fit parameters

FDG Model	***V_a (%)***	***τ (min)***	***K_1 (min^{-1})***	***k_2 (min^{-1})***	***k_3 (min^{-1})***
Prostate	*5,78*	*0,78*	0,35 ± 7%	0,41 ± 5%	0,0011 ± 6%
- direct	15,5 ± 23%	0,97 ± 6%	0,26 ± 10%	0,28 ± 11%	0,0010 ± 7%
Spot 1	*5,78*	*0,78*	0,40 ± 12%	0,27 ± 5%	0,0030 ± 3%
- direct	24,7 ± 42%	1,01 ± 8%	0,36 ± 19%	0,23 ± 16%	0,0033 ± 6%
Spot 2	*5,78*	*0,78*	0,30 ± 12%	0,16 ± 3%	0,0038 ± 6%
- direct	37,3 ± 32%	1,16 ± 33%	0,24 ± 25%	0,09 ± 26%	0,0030 ± 9%
	#parameters	**cAIC**	**BIC**	**MSE**	
Prostate	5	-151,55	-146,53	0,0060	
Spot 1	5	-79,61	-74,59	0,0566	
Spot 2	5	-64,76	-59,74	0,0890	

**cursive values were obtained from the whole prostate fit*

1.5. 2 Compartment Model

Figure 8 displays the 2 compartment fits for the three VOIs while Table 4 contains the corresponding fit parameters and information criteria.

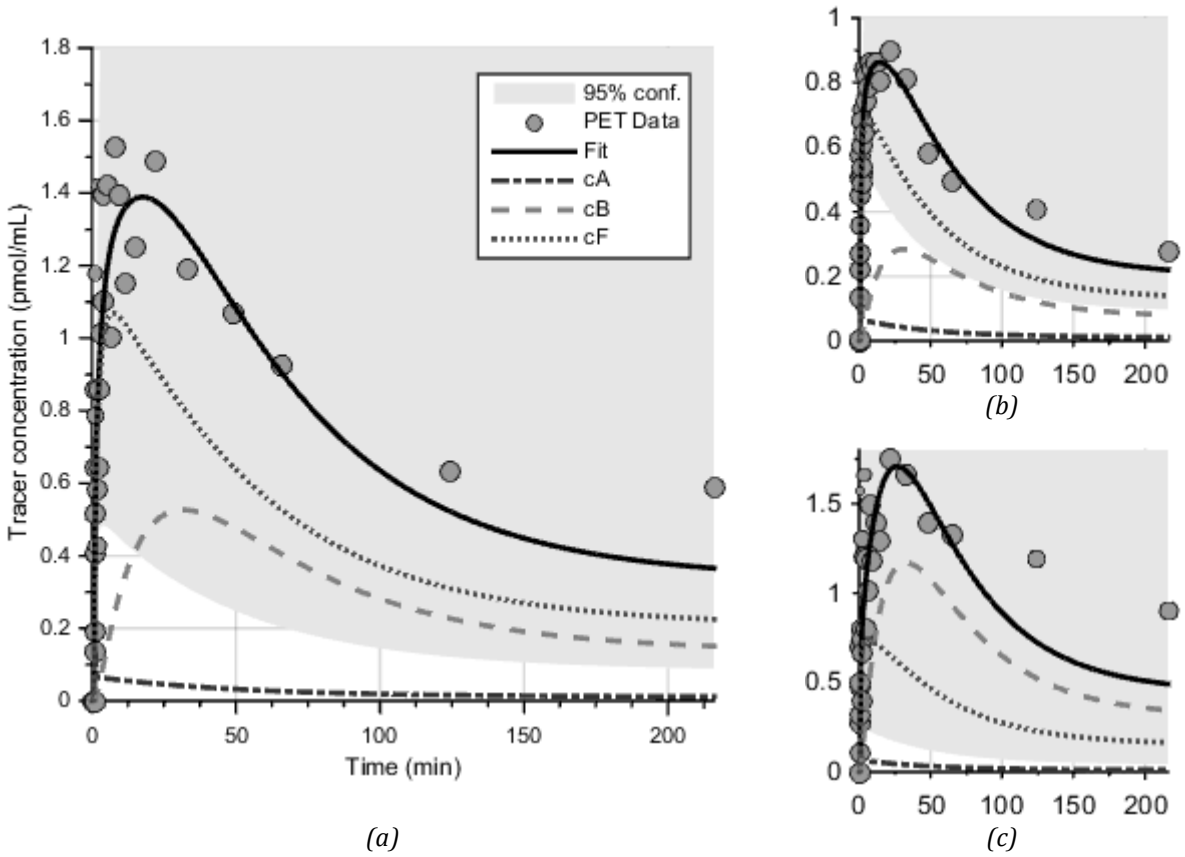

Figure 8: 2 Compartment fit of the first spot (a), the whole prostate (b) and the second spot (c)

Table 4: 2 Compartment fit parameters

2-Comp.	***V_a (%)***	***τ (min)***	***K_1 (min^{-1})***	***k_2 (min^{-1})***	***k_3 (min^{-1})***	***k_4 (min^{-1})***
Prostate	*5,78*	*0,78*	0,40 ± 15%	0,59 ± 31%	0,04 ± 129%	0,07 ± 100%
- direct	6,1 ± 122%	0,81 ± 16%	0,41 ± 26%	0,61 ± 44%	0,04 ± 136%	0,07 ± 102%
Spot 1	*5,78*	*0,78*	0,53 ± 37%	0,48 ± 70%	0,46 ± 131%	*0,07*
- direct	23,6 ± 54%	1,01 ± 9%	0,38 ± 50%	0,25 ± 81%	0,01 ± 307%	0,01 ± 509%
Spot 2	*5,78*	*0,78*	0,57 ± 55%	0,70 ± 114%	0,14 ± 109%	*0,07*
- direct	11,6 ± 173%	1,01 ± 17%	0,59 ± 62%	0,54 ± 95%	0,04 ± 108%	0,02 ± 106%
	#parameters	**cAIC**	**BIC**	**MSE**		
Prostate	6	-162,10	-156,67	0,0039		
Spot 1	6	-73,34	-67,90	0,0626		
Spot 2	6	-66,95	-61,52	0,0764		

**cursive values were obtained from the whole prostate fit*

1.6. Linearized Models

The linearized models by Patlak and Logan of the prostate and both spots are given in Figure 9 and Figure 10, with the respective parameters in Table 5 and Table 6. Both tables in addition contain the slope parameters as calculated using the transfer coefficients from the compartment model fits.

1.6.1. Patlak Plot

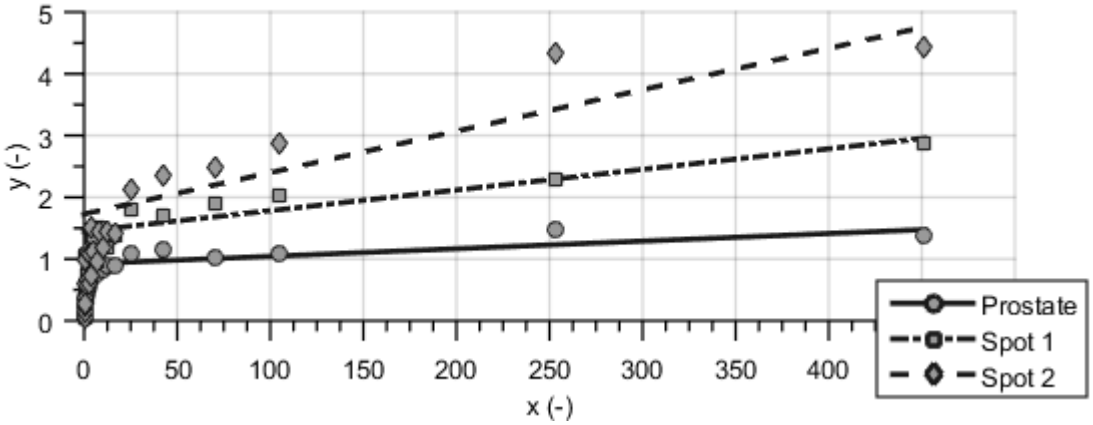

Figure 9: Patlak plot of three VOIs

Table 5: Patlak plot parameters

Patlak	***A (-)***	***B (min^{-1})***	***B_{comp} (min^{-1})***
Prostate	0,92 ± 5%	0,0012 ± 23%	0,00094 ± 19%
Spot 1	1,45 ± 5%	0,0033 ± 11%	0,0044 ± 21%
Spot 2	1,73 ± 8%	0,0078 ± 9%	0,0070 ± 22%

1.6.2. Logan Plot

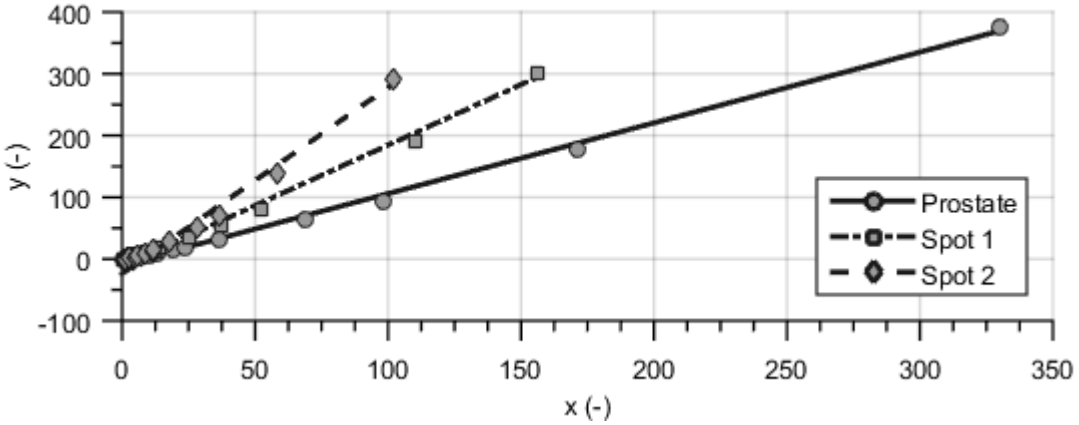

Figure 10: Logan plot of the three VOIs

Table 6: Logan plot parameters

Logan	***k_2 (min)***	***V_d (-)***	***$V_{d,comp}$ (-)***
Prostate	0,11 ± 14%	1,15 ± 1%	1,07 ± 634%
Spot 1	0,09 ± 15%	1,96 ± 1%	8,36 ± 653%
Spot 2	0,04 ± 12%	3,02 ± 2%	2,44 ± 1021%

2. *Monte Carlo and AIF Validation*

2.1. Siemens Biograph mCT Model Performance

Figure 11 displays the number of trues, scatters and randoms as function of activity in the FOV during the calibration simulation and the respective FBP reconstruction. The sensitivity and scatter fraction for the calibration source were respectively 11,1 ± 0,027 kcps/MBq and 14,42 ± 0,02%, while the measured activity was found to be too low to determine the NECR peak. The calibration factor for the femoral phantom was 220 ± 5,81 Bq/cps. An overview of the spatial resolution at different locations in the FOV is given in Table 2.

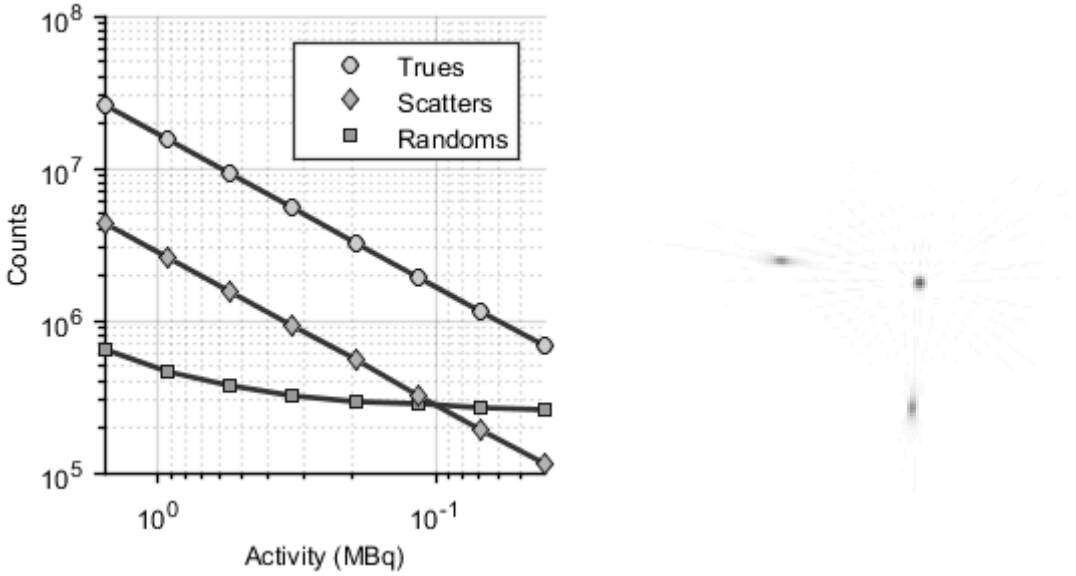

Figure 11: *(left) The number of trues, scatters and randoms as function of activity for the Siemens Biograph mCT model. (right) Non-calibrated reconstruction of the spatial resolution simulation*

Table 7: Siemens Biograph mCT simulation model spatial resolution with the values reported by Jakoby[23] *between brackets*

(x,y,z)	x (mm FWHM)	y (mm FWHM)	z (mm FWHM)
(10,0,0) cm	5,51 ± 0,99	3,96 ± 0,53	3,78 ± 0,54
(0,1,0) cm	4,00 ± 0,56 (4,4)	4,00 ± 0,56	3,83 ± 0,92
(0,10,0) cm	3,96 ± 0,53 (4,7)	5,55 ± 1,02 (5,7)	3,78 ± 0,54 (5,9)
(0,0,1) cm	4,00 ± 0,56	4,00 ± 0,56	3,92 ± 0,54
(0,0,5) cm	3,99 ± 0,56	3,99 ± 0,56	3,86 ± 0,53

2.2. Arterial Input Function Validation

2.2.1. Input Functions

The decay corrected arterial and venous input TACs are shown in Figure 12 with the respective tri-exponential parameters given in Table 8. The difference between the arterial and venous concentration was below 10% after 60 minutes for all generated functions.

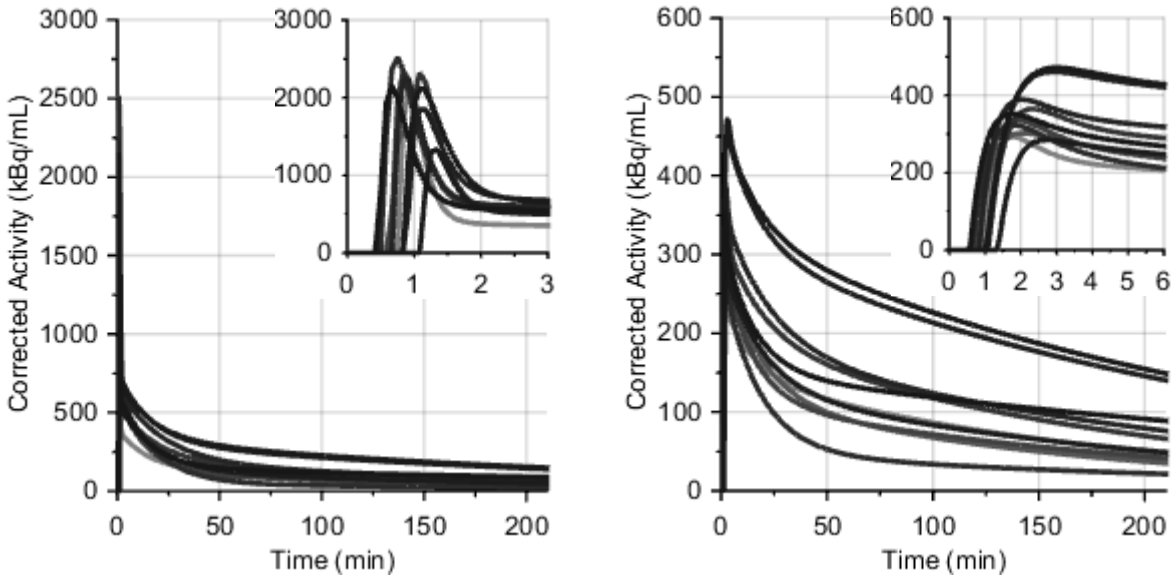

Figure 12: Plots of the generated AIFs (left) and VIFs (right)

Table 8: AIF and VIF tri-exponential parameters

#fun		A_1 (kBq/mL)	A_2 (kBq/mL)	A_3 (kBq/mL)	L_1 (min^{-1})	L_2 (min^{-1})	L_3 (min^{-1})	τ (min)
1	AIF	36836	240	149	7,19	0,073	0,0055	0,77
	VIF	656	89	149	1,96	0,073	0,0055	0,94
2	AIF	20078	477	120	6,25	0,059	0,0059	0,64
	VIF	357	177	120	1,71	0,059	0,0059	0,79
3	AIF	30884	483	116	5,79	0,074	0,0049	0,66
	VIF	550	180	116	1,58	0,074	0,0049	0,81
4	AIF	29297	342	196	5,46	0,056	0,0052	0,89
	VIF	521	127	196	1,49	0,056	0,0052	1,09
5	AIF	29255	597	49	5,11	0,059	0,0040	0,52
	VIF	521	222	49	1,39	0,059	0,0040	0,64
6	AIF	30715	459	187	6,05	0,046	0,0043	0,69
	VIF	547	171	187	1,65	0,046	0,0043	0,84
7	AIF	19178	422	310	5,07	0,063	0,0038	0,89
	VIF	341	157	310	1,38	0,063	0,0038	1,09
8	AIF	16691	406	133	6,18	0,056	0,0048	1,11
	VIF	297	151	133	1,69	0,056	0,0048	1,37
9	AIF	19689	372	329	4,32	0,062	0,0038	0,84
	VIF	350	138	329	1,18	0,062	0,0038	1,04
10	AIF	28155	465	153	5,89	0,073	0,0026	0,47
	VIF	501	173	153	1,61	0,073	0,0026	0,58

2.2.2. Correction method comparison

The relative errors over time, as given by equation 5, for each correction method are given in Figure 13. Both Chen and Hackett proved to be very sensitive to the initial values of the least squares regression and required a large number of iterations with varying initial values to estimate the global minimum. Based on this data, Hackett's method was chosen as correction method for the patient data.

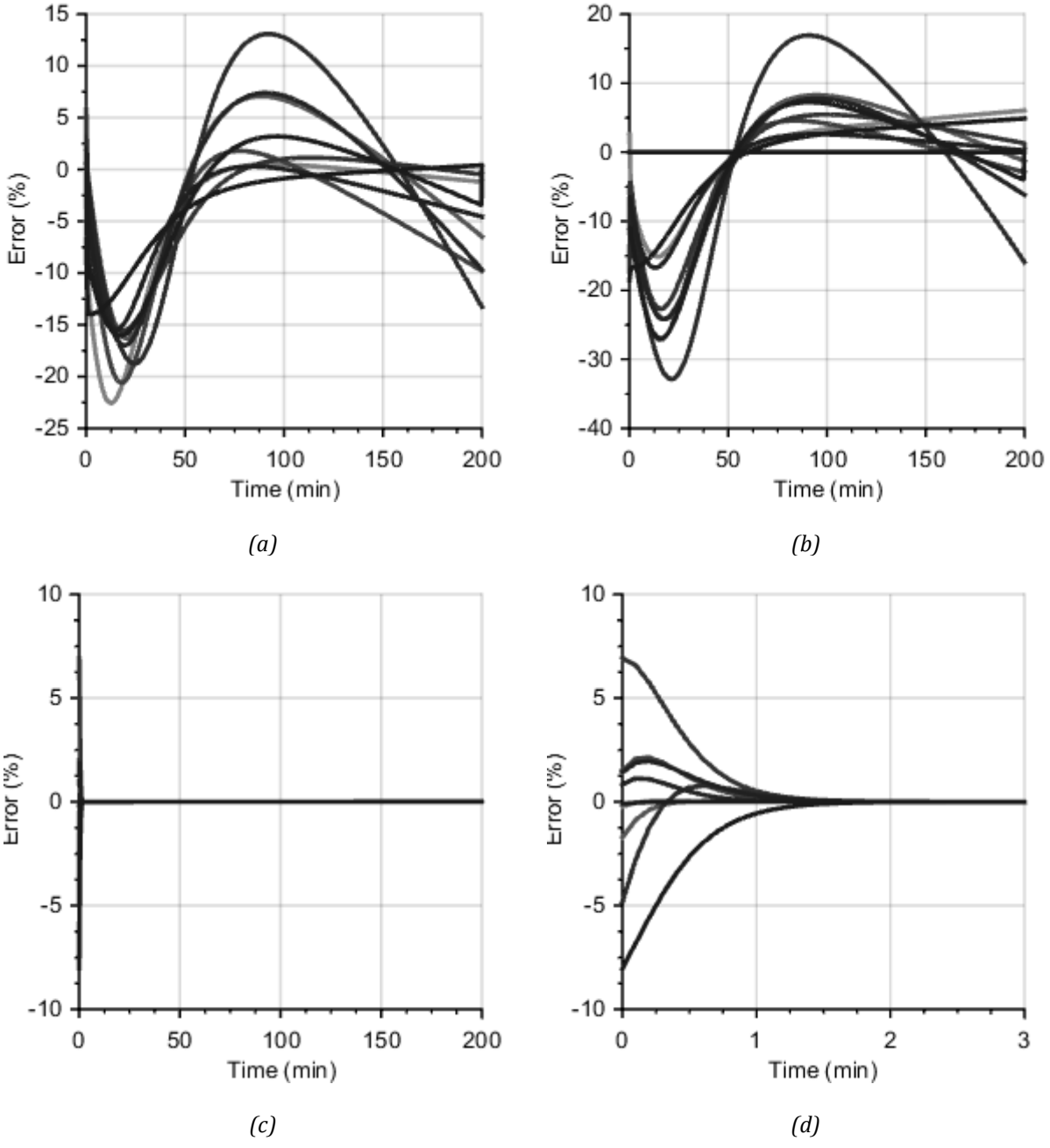

Figure 13: Relative error of the calculated AIF compared to the initial input for Chen's method (a), Mourik's method (b), Hackett's method (c) and Hackett's method zoomed in on the few first minutes (d)

3. Dosimetry

The calculated TTCs are given in Figure 14 and the bladder TTC approximation is shown in Figure 15. Due to the small dataset, the 95% confidence intervals were large and the resulting confidence areas were too large to display. The kidney perfusion factor was estimated at 0,0031 min^{-1}.

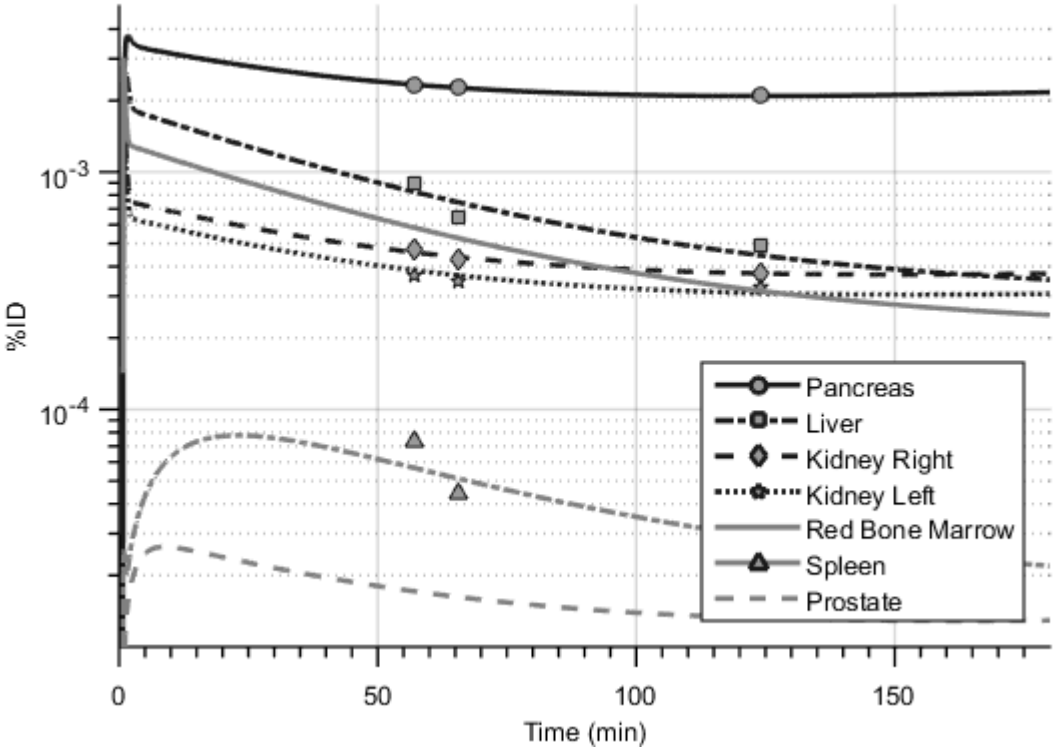

Figure 14: Approximations of the primary organ TTCs

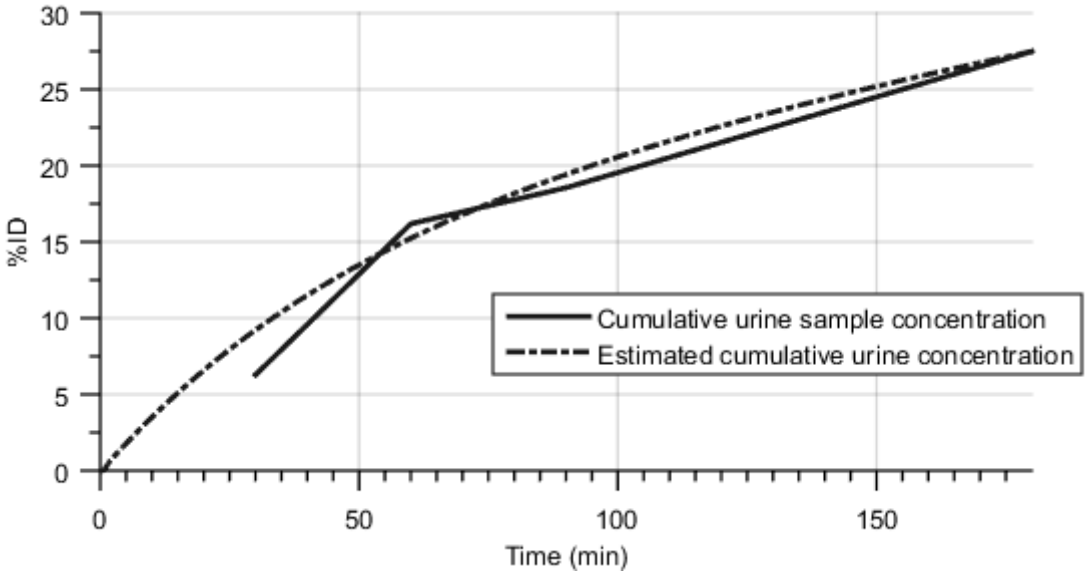

Figure 15: Estimation of the bladder filling using a perfusion model and the cumulative urine sample concentrations

Supplying this data to OLINDA/MEX using the ICRP60 1990 weighting factors yielded the following dose estimates:

Table 9: OLINDA/MEX ICRP60 1990 organ doses

Organ	***mBq-h/Bq***	***Absorbed Dose (µGy/MBq)***	***Effective Dose (µSv/MBq)***
Liver	14,1	6,19	0,310
Kidneys	11,9	20,2	0,101
Spleen	1,41	6,11	0,036
Pancreas	25,0	139	0,696
Prostate	0,59	16,5	3,30
Red bone marrow	7,68	11,6	1,39
Bladder	160	196	9,82
Whole body	1420	13,0	-
Residual			6,75
Total	**1640**		**22,40**

Discussion

1. Monte Carlo and AIF Validation

1.1. Siemens Biograph mCT Model Performance

The first goal of this project was to compare and evaluate the IDIF correction methods proposed by Chen, Mourik and Hackett. Since arterial sampling was not possible, a Monte Carlo approach was used. A model of the Siemens Biograph mCT was built in GATE v7.0. However, since some of the specification, like the delay window and more advanced crystal characteristics, were proprietary, it was not possible to build an exact model. Despite these limitations, the sensitivity was comparable with 13% overestimation compared to the experimental results[23]. The spatial resolutions in the transaxial and radial were respectively 10% and 3% higher. This can be attributed to the lack of more advanced factors like light sharing and individual crystal sensitivity[24]. The axial resolution was almost two times larger than reported by Jakoby. This was likely due to a combination of the earlier mentioned factors, removing the gap between the detector blocks and reconstruction without axial or angular compression. Since the vessels in the AIF simulation were placed parallel to the axial axis, the axial resolution overestimation was not expected to influence the results of the AIF validation study.

1.2. Arterial Input Function Validation

Both Chen and Mourik's methods showed significant under- and overestimation at respectively 20 and 90 minutes post-injection. It was found that both these methods were vulnerable to errors in the concentration measurements. Also, Chen's method uses the venous samples to calculate the spillover from the surrounding tissue into the artery. Since the concentration of the surrounding tissue, in this case given by the venous concentration, was the same as the arterial concentration at the times of the venous samples, it was not possible to calculate the spillover factor. The fits were therefore made with a 5% overspill factor, a value based on the spatial resolution of the scanner model. While both methods performed well in ideal situations, it was concluded that these methods were too unreliably for experimental data. Based on the original articles, it was expected that Chen would perform the best. However, all these articles were based on the carotid artery. The increased overspill and recovery coefficient showed to be in favor of Hackett's method.

Hackett's method gave very good results in the validation study. Since this method weighs the venous samples much higher compared to Chen and Mourik, the errors after the first-pass peak were negligible. However, since the height of the peak was determined by the measured blood fraction in the VOI, this method was prone to bias error during the first-pass peak. Due to the brief time span of the error, this bias error mainly influences the calculated blood fraction V_a in the target VOI and the perfusion factors, but has little effect on the k_3 parameter. For example, increasing the height of the peak by 100% only let to a 10% increase in k_3 in the direct fit of a FDG model on the whole prostate while the blood fraction almost doubled.

2. Pharmacokinetic Modeling

Three compartment models were fit to the whole prostate and the two spot suspicious of cancerous tissue displayed in Figure 4. It was found that the models were sensitive to the initial values, often leading to significant bias error when all parameters were fitted directly. This effect became clear during direct fitting of the FDG model where unrealistic fitted blood fractions of 25% to 37% were observed in the spots. The large number of global minima due to the large

number of parameters compared to the small dataset made it almost impossible to find the global solution. The variance reducing procedure mentioned in Materials and Methods 2.3 proved to be effective in minimizing the number of variables by precalculating the blood fraction and time delay. This led a decrease in bias error. It was found that the global minimum was best found by first fitting all the parameters directly and using the resulting values as initial values for the variance reducing procedure.

2.1. Model Comparison

First a fit over the early samples of the whole prostate was made to determine the blood fraction and time delay. The blood fraction was 5,78% ± 52%, which matched Inaba's value of 6,1% closely[25]. The leading physician expected that the spots were too small to observe significant angiogenesis and this value was therefore also used for fitting of the spots. The time delay was 47 seconds, which was 6 seconds later compared to the time delay found in the femoral artery. This was as expected since the blood travels significantly lower in the capillaries[26] and reconstruction fails at very low activity levels. The 1 compartment model, or simple perfusion, was unable to describe the whole curve for all VOIs since it underestimated the concentration 50 minutes post-injection as shown in Figure 6. The relatively large uncertainty in the blood fraction in the whole prostate was caused by the large variance in the first few frames of the dynamic scan due the small number of counts in these frames. The variance reducing procedure was only minimally effective in reducing the variance.

While the information criteria were too inconsistent, visual inspection and parameter uncertainty favored the FDG model for [^{68}Ga]Sarabesin 3. Predetermination of the blood fraction and time delay were paramount as direct fitting led to too many local minima and bias error in these variables. The slope parameters calculated using the Patlak plot, which are considered to be more robust, showed to be in gross accordance with the slope parameters calculated from the compartment model fits as shown in Table 5 and *Table 6*. However, the existing difference between these values suggest that there is still room for improvement for the bias error. The k_3 parameters in the spots was found to be 2,7 to 3,5 times higher than in the whole prostate. The increased receptor concentrations in the spots were also found in the Logan and Patlak plot. The introduction of the retention parameter in the 2 compartment model led to a large increase in uncertainty and fitting mismatch and two minima were found, one with a relatively large k_4 as displayed in Figure 7 and one where $k_4 \approx 0$, which is a FDG model. The variance reducing procedure showed a significant decrease in bias error.

Based on the accuracy of the Logan plot compared to the Patlak plot, a 2 compartment model with a small k_4 parameter was an alternative. However, it was not possible to isolate this solution due to the small number of measurement points 50 minutes post-injection and the relatively large noise contribution. These results are a strong argument for the effectiveness of [^{68}Ga]Sarabesin 3 in targeting GPRr in tissue. A high uptake and retention was observed in areas with GPRr expression and a clear contrast was observed between healthy prostate tissue and areas suspicious of cancerous tissue.

The (near-)FDG model and low metabolism in the blood is favorable for both imaging and therapy using [^{68}Ga]Sarabesin 3. The high retention in organs with GRPr expression allows for high doses in the target volumes compared to the healthy tissue when using isotopes with relatively long half-lifes. The high retention also means that the tumor-to-healthy tissue ratio will increase over time during imaging. However, due to the shorter half-lifes of the isotopes

used for imaging, a trade-off between contrast and image quality, based on the number of coincidences, must be made. It is advisable to order the patient to void his bladder before imaging to limit the interference by the hot bladder.

2.2. Quantitative Pharmacokinetic Modeling Considerations

A number of factors have been observed that limited the accuracy and reliability of the quantitative results of this pharmacokinetic analyses. Firstly, while Hackett's method showed promising results in the Monte Carlo simulation, it is not known how well this holds in vivo. While it can be argued that the error contribution of the AIF was probably small, the exact uncertainty was unknown. Secondly, due the small size of the spots, PVEs are significant. Rewriting the 2 compartment model equations given in APPENDIX A : Compartment models and Linearizations [9] to include the recovery coefficients gives insight in how PVE affects the compartment analyses.

In the first scenario it was assumed that the measured and true tissue concentrations, respectively $c_{T,true}$ and $c_{T,meas}$, are much larger than the background:

$$rc = \frac{c_{T,meas} - c_{bg}}{c_{T,true} - c_{bg}} \approx \frac{c_{T,meas}}{c_{T,true}} \tag{6}$$

Where c_{bg} is the background concentration and rc is the recovery coefficient. In this case the recovery coefficient is independent of time:

$$\frac{\partial rc}{\partial t} = 0 \tag{7}$$

The measured concentration can then be written as

$$c_{T,meas} = rc \cdot c_{T,true} = \left(rc \cdot V_{a,true}\right) \cdot c_a + rc \cdot c_{b,true} + rc \cdot c_{f,true} \tag{8}$$

$$\frac{\partial c_{T,meas}}{\partial t} = V_{a,meas} \cdot c_a' + c_{b,meas}' + c_{f,meas}' \tag{9}$$

Where $V_{a,true}$ is the true blood fraction, $V_{a,meas}$ is the measured blood fraction, $c_{b,true}$ is the true bound concentration and $c_{f,true}$ is the true free concentration. The derivate of the bound concentration is given by

$$\begin{aligned} c_{b,meas}' = \frac{\partial\left(rc \cdot c_{b,true}\right)}{\partial t} &= -rc \cdot k_4 \cdot c_{b,true} + rc \cdot k_3 \cdot c_{f,true} \\ \rightarrow c_{b,meas}' &= rc \cdot \left[-k_4 \cdot c_{b,true} + k_3 \cdot c_{f,true}\right] \end{aligned} \tag{10}$$

and the derivate of the free concentration is calculated in a similar matter

$$\begin{aligned} c_{f,meas}' = \frac{\partial\left(rc \cdot c_{f,true}\right)}{\partial t} &= -rc \cdot (k_2 + k_3) \cdot c_{f,true} + rc \cdot k_4 \cdot c_{b,true} + k_1 \cdot c_a \\ \rightarrow c_{f,meas}' &= rc \cdot \left[-(k_2 + k_3) \cdot c_{f,true} + k_4 \cdot c_{b,true} + rc^{-1} \cdot k_1 \cdot c_a\right] \end{aligned} \tag{11}$$

Recombining these derivatives with equation 9 yields:

$$\begin{aligned}\frac{\partial c_{T,meas}}{\partial t} &= rc \cdot \frac{\partial c_{T,true}}{\partial t} = V_{a,meas} \cdot c_a' + rc \cdot \left[-k_4 \cdot c_b + k_3 \cdot c_f\right] + rc \\ &\cdot \left[-(k_2 + k_3) \cdot c_{f,true} + k_4 \cdot c_{b,true} + rc^{-1} \cdot k_1 \cdot c_a\right] \\ = rc \cdot \left[rc^{-1} \cdot V_{a,meas} \cdot c_a' + -k_4 \cdot c_{b,true} + k_3 \cdot c_{f,true} + -(k_2 + k_3) \cdot c_{f,true} + k_4 \cdot c_{b,true}\right. \\ &\left. + rc^{-1} \cdot k_1 \cdot c_a\right]\end{aligned} \quad 12$$

Comparing this to the true concentration given in equation 8, one can conclude that $V_{a,meas} = rc \cdot V_{a,true}$, $k_{1,meas} = rc \cdot k_{1,true}$ and that the transfer coefficients k_2, k_3 and k_4 are independent of the recovery coefficient. Therefore, in cases where the background is negligible compared to the spot, the k_3 parameter and retention coefficient can be accurately determined despite PVEs. However, in this study this assumption is not reasonable. It is therefore better to write:

$$rc = \frac{c_{T,meas} - c_{bg}}{c_{T,true} - c_{bg}} \approx \frac{c_{T,meas} - c_{bg}}{c_{T,true}} \quad 13$$

Equation 8 then changes to

$$c_{T,meas} - c_{bg} = rc \cdot c_{T,true} = \left(rc \cdot V_{a,true}\right) \cdot c_a + rc \cdot c_{b,true} + rc \cdot c_{f,true} \quad 14$$

$$\frac{\partial\left(c_{T,meas} - c_{bg}\right)}{\partial t} = V_{a,meas} \cdot c_a' + c_{b,meas}' + c_{f,meas}' \quad 15$$

These equations can be solved similarly to the first case if the recovery coefficient is independent of time

$$\frac{\partial rc}{\partial t} = \frac{c_{T,meas}' \cdot c_{T,true} - c_{T,true}' \cdot c_{T,meas} + c_{T,meas}' \cdot c_{bg} - c_{bg}' \cdot c_{T,true}}{c_{T,true}^2} = 0 \quad 16$$

This is the case when:

$$c_{T,meas}' \cdot c_{T,true} - c_{T,true}' \cdot c_{T,meas} = 0 \quad 17$$

and

$$c_{T,meas}' \cdot c_{bg} - c_{bg}' \cdot c_{T,true} = 0 \quad 18$$

In order for equations 17 and 18 to hold, both the measured concentration and the background should be proportional to true concentration in the form of

$$c_{T,meas} = \alpha \cdot c_{T,true} \quad 19$$

$$c_{bg} = \beta \cdot c_{T,true} \quad 20$$

This is obviously true for the measured concentration, but not for the background, since even with specific uptake in the background, the receptor density would be far lower. Since the spot-to-background ratio increased during the measurement due to the high specific uptake in the spots, the recovery coefficient was expected to increase over time. This increase was not quantifiable due to the unknown true concentration and it was therefore unknown how much this affected the fitting parameters. Combining these arguments, it was expected that the current study was not reliable enough for exact quantification of receptor densities in the target volumes. However this study yields enough information for qualitative assessment of the

effectiveness of the tracer and quantitative comparison between spots of similar size and spot-to-background ratio. In vivo validation of Hackett's method, large spot-to-background ratios and more PET measurements 50 minutes post-injection are required for reliable quantitative pharmacokinetic analyses.

3. Dosimetry

The small dataset for the primary organs only allowed for a gross estimation of the absorbed dose since factors like the blood-to-red bone marrow concentration ratio and uptake in regions outside the abdomen were unknown. It was found that the liver and spleen followed a 1 compartment model while the kidneys and pancreas better fitted to a FDG model. Due to the relatively short half-life of the isotope, most of the disintegrations occurred in the blood and during early perfusion resulting in only 14% of the disintegrations occurring in the primary organs given in Table 9. The simple one-way perfusion model for the bladder filling proposed in Materials and Methods section 3 matched the measured urine samples concentration well. The primary organs at risk are the bladder, the red bone marrow and the prostate. The bladder absorbed dose of 196 µGy/MBq was similar comparted to the [^{18}F]DG dose reported by Hays[14]. The effective dose of 22,40 µSv/MBq was comparable to the 19 µSv/MBq for [^{18}F]DG[27].

3.1. Comparison to other Galium-68 tracers

The doses for 4 Gallium-68 are given in Table 10 for comparison with the values calculated for [^{68}Ga]Sarabesin 3.

Table 10: Organ doses for different Gallium-68 tracers given in µSv/MBq, with the target receptor given between brackets.

Organ	***Pentixafor*** [28] ***(CXCR4)***	***DOTATAC*** [29] ***(SSTR)***	***DOTATATE*** [29] ***(SSTR)***	***PSMA-IT*** [30] ***(PSMA)***	***Sarabesin 3 (GRP)***
Liver	17,5	41,0	50,0	43,1	6,19
Kidneys	35,0	82,0	93,0	22,0	20,2
Spleen	53,8	108	109	63,4	6,11
Pancreas	12,8	-	-	13,2	139
Bladder	81,4	119	98,0	67,4	196
Effective Dose Coefficient	15,6	21,0	21,0	19,9	22,4

It can be seen that, despite the differences in organ-specific absorbed doses due to the different pharmacokinetics between the tracers, the effective dose coefficient of [^{68}Ga]Sarabesin 3 is in close comparison with the other tracers. Both the pancreas and the bladder show a higher dose for [^{68}Ga]Sarabesin 3. While the increased pancreas dose is as expected, it will be a limiting factor for treatment with this tracer. The lower uptake in the other organs can however be beneficial. It can therefore be argued that Sarabesin 3 is safe for diagnostic applications, but requires further study before it can be used therapeutically.

Conclusion

Despite the small spots in the prostate, suboptimal measurement time frames and an IDIF, the combination of step-wise IRLS fitting and a Monte Carlo validated AIF correction method led to an accurate description of the [^{68}Ga]Sarabesin 3's behavior in healthy tissue and tissue suspicious of cancer tissue. It was found that the tracer follows an FDG model or a 2 compartment model with a small k_4 parameter that approximates the FDG model. It was not possible to exactly determine this latter parameter due to the relatively high noise and small number of measurement points 50 minutes post-injection. The k_3 parameters for respectively the whole prostate, the first and second spot were 0,0011 ± 6%, 0,0030 ± 3% and 0,0038 ± 6%. While the errors are low, one should note that these are the fitting errors that do not include the AIF and measurement errors.

Using Monte Carlo simulations, three AIF correction methods were evaluated by applying these to a set of randomly generated arterial and venous concentration curves in a model of the Siemens Biograph mCT scanner in GATE v7.0. It was found that both Chen and Mourik's method were prone to errors in the measurement points and that Chen's overspill factor estimation was invalidated due to the equal concentrations in the vein and artery at the estimation time points. Hackett's method showed very good results after the initial peak, but remains vulnerable to bias error due to miscalculation of the blood volume in the VOI. However, this bias error mainly affects the perfusion and blood fraction parameters and has little effect on the estimated k_3 parameter.
The effective dose and absorbed dose in the bladder by [^{68}Ga]Sarabesin 3 were similar to [^{18}F]DG and other Gallium-68 tracers with respectively 22,40 µSv/MBq and 196 µSv/MBq. The simple one-way perfusion model of the kidney showed to be in good accordance with the measured urine samples.

In conclusion, [^{68}Ga]Sarabesin 3 showed a strong specific uptake in targets with GRPr expression. Despite being an antagonist, the disassociation coefficient was too small to measure and the behavior was well approximated using a FDG model. A good contrast was observed between the healthy prostate tissue and spots suspicious of cancerous tissue. [^{68}Ga]Sarabesin 3 can therefore be a good candidate for both imaging and treatment of prostate cancer. It is expected that [^{68}Ga]Sarabesin 3 is safe for the patient with an estimated effective dose that only slighted exceeds that of [^{18}F]DG.

Acknowledgements

This work would have not been possible without the help and guidance from my supervisors M. Segbers and M. Konijnenberg. I am very grateful for the opportunities, great experiences and trust they have granted me during this thesis. I would also like to thank I. Bakker for sharing her expertise and enthusiasm for this subject and the nuclear medicine team for providing the data for this thesis.

Furthermore, I received much help from the international Gate and STIR communities. Special mentions are Michael Fieseler from the University of Münster, David Sarrut, Tristan Glatard and Sorina Camarasu-Pop from the VIP team at the Institut national des sciences Appliquées de Lyon and Valerio Tabacchini from the Delft University of Technology.

I would also like to thank A. Denkova for her supervision from Delft.

APPENDIX A : Compartment models and Linearizations [9]

Pharmacokinetic modeling is a way to describe the kinetics, or behaviour, of a pharmacon. A good pharmacokinetic model improves the understanding of the pharmacon and can yield information about the tissue that is studied[31]–[33].

1.1. Compartment Modeling

1.1.1. Mathematical Background

Compartment modeling tries to describe the behaviour of the tracer by dividing the different physiological states into different compartments. These compartments interact with each other via so called transfer rates, given in s^{-1}. The simplest compartment model consists of single compartment connected to an arterial input c_a. An illustration is given below. Here is c_a the tracer concentration in the blood and c_t the tracer concentration in the tissue.

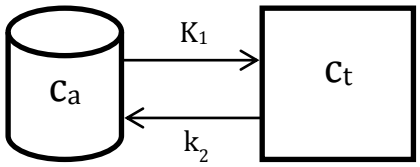

Figure 16: One compartment model

It is clear that the concentration in the tissue follows from the equation below:

$$\frac{dc_t}{dt} = K_1 \cdot c_a - k_2 \cdot c_t \qquad 21$$

Here c_a and c_t are respectively the arterial and tissue concentration and K_1 and k_2 are the transfer coefficients. Since the arterial concentration is not always analytically defined, it is more compelling to write the above equation as a convolution[9]:

$$c_t(t) = K_1 e^{-k_2 t} * c_a(t) \qquad 22$$

The resulting signal in the VOI will comprise of both tissue and the blood concentration, as given in the equation below:

$$c_{tot}(t) = V_a \cdot c_a(t) + (1 - V_a) \cdot c_t(t) \qquad 23$$

where V_a is the blood fraction in the VOI. By fitting this equation, the transfer coefficients can be obtained. This simple model can be expanded by adding more compartments for e.g. bound ligands or metabolites.

1.1.2. Two compartment model

The two compartment model splits the tissue concentration into a free ligand and bound ligand concentration by adding another compartment after the free ligand compartment. A schematic is given in Figure 17. Here is c_f the free (non-bound) tracer concentration and c_b the bound tracer concentration. The total tissue concentration is given by $c_t = c_a + c_b$.

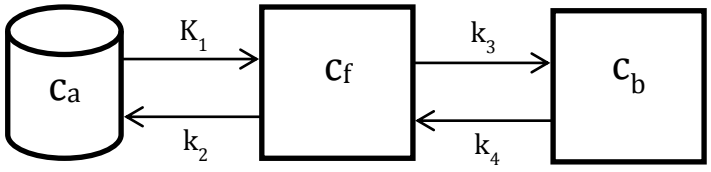

Figure 17: Two compartment model

The equations for both compartments now are:

$$\frac{dc_f}{dt} = K_1 \cdot c_a + k_4 \cdot c_b - (k_2 + k_3) \cdot c_f \quad (24)$$

$$\frac{dc_b}{dt} = k_3 \cdot c_f - k_4 \cdot c_b \quad (25)$$

Solving this equations is done using a system on linear differential equations. Assuming exponential decay, the factors can be found using eigenvalue analysis of the system. Since solving these equations is quite an elaborate process only the solution will be shown.

$$c_f = \frac{K_1}{\alpha_2 - \alpha_1}[(k_4 - \alpha_1) \cdot e^{-\alpha_1 t} + (\alpha_2 - k_4) \cdot e^{-\alpha_2 t}] \quad (26)$$

$$c_b = \frac{K_1 k_3}{\alpha_2 - \alpha_1}(e^{-\alpha_1 t} - e^{-\alpha_2 t}) \quad (27)$$

$$c_t = \frac{K_1}{\alpha_2 - \alpha_1}[(k_3 + k_4 - \alpha_1) \cdot e^{-\alpha_1 t} + (\alpha_2 - k_3 - k_4) \cdot e^{-\alpha_2 t}] \quad (28)$$

Where α_1 and α_2 are derived from:

$$\alpha^2 - \alpha(k_2 + k_3 + k_4) + k_2 k_4 = 0 \quad (29)$$

1.1.3. FDG model

The FDG model is very similar to the 2 compartment model. It also takes specific binding into account, but assumes that the retention is indefinite and k_4 is therefore 0.

1.1.4. Resulting variables

Kinetic modeling allows for measurement of a variety of quantities, some of which will be described here. All these values are derived for a two compartment model. First the following definitions:

$$k_3 = k_{on} f_{ND} \left(B_{max} - \frac{C_b(t)}{SA} \right) \quad (30)$$

$$k_4 = k_{off} \quad (31)$$

Where B_{max} is the receptor concentration, k_{on} and k_{off} respectively the association and dissociation rate constants, SA the specific activity of the, and f_{ND} the free fraction of ligands in the tissue. When c_b / SA is small comparted to B_{max}, k_3 simplifies to a time-invariant function. In this case the equilibrium dissociation constant K_d and the binding potential can be defined as:

$$K_d = {k_{off}}/{k_{on}} \quad (32)$$

$$k_3/_{k_4} = BP_{ND} = f_{ND}\, B_{max}/_{K_d} \quad (33)$$

1.2. Linearizations: Patlak

Linearizations offer a more robust fitting method compared to compartment model at the cost of inseparability of the distinct transfer coefficients found in compartment models. The Patlak plot is a linearization of the FDG model which transforms the tissue concentration equation in the form of $y = a + b \cdot x$. The resulting Patlak equation is given below. The full derivation can be found in [9].

$$\frac{c_t}{c_a} = \frac{K_1 k_2}{(k_2 + k_3)^2} + \frac{K_1 k_3}{k_2 + k_3} \frac{\int_0^t c_a \, d\tau}{c_a} \quad (34)$$

Where the latter constant is the most important constant which represent the uptake of the tracer in the tissue.

1.3. Linearizations: Logan

The Logan plot is similar to the Patlak plot, but instead describes the complete 2 compartment model instead of the FDG model used by Patlak. The equation for the Logan plot is given below. The full derivation can again be found in [9].

$$\frac{\int_0^t c_t \, d\tau}{c_t} = -\frac{k_3 + k_4}{k_2 k_4} + K_1 \frac{k_3 + k_4}{k_2 k_4} \frac{\int_0^t c_a \, d\tau}{c_t} \quad (35)$$

Where the latter constant is known as the volume of distribution.

APPENDIX B : ANALYTICAL SOLUTION 2 COMPARTMENT MODEL

MATLAB Symbolic Toolbox code:

```
syms ct(t) cb(t) cf(t)
syms k1 Vd k3 k4 t positive
syms A1 A2 A3 L1 L2 L3 positive

syms sol_k3 cpet cpet_u k1_u Vd_u k3_u k4_u positive

sol_ct = dsolve(...
    diff(cb) == -k4*cb + k3*cf, ...
    diff(cf) == k4*cb - (k1/Vd + k3)*cf + k1*((A1*t-A2-A3)*exp(-L1*t) +
A2*exp(-L2*t) + A3*exp(-L3*t)),...
    cf(0) == 0, cb(0) == 0,'IgnoreAnalyticConstraints',true);
```

Some manual adjustments were made to cancel out a number of exponentials in the solution in order to prevent infinities during numerical evaluations.

Analytical solution:

```
c_bound(t) = ((k1*k3*exp(-(t*(k2 + k3 + k4 - (k2^2 + 2*k2*k3 - 2*k2*k4 + k3^2
+ 2*k3*k4 + k4^2)^(1/2)))/2)*(A1*((2*exp((k2*tau)/2 + (k3*tau)/2 +
(k4*tau)/2 - (tau*(k2^2 + 2*k2*k3 - 2*k2*k4 + k3^2 + 2*k3*k4 +
k4^2)^(1/2)))/2)*(2*L1*tau - k2*tau - k3*tau - k4*tau + tau*(k2^2 + 2*k2*k3
- 2*k2*k4 + k3^2 + 2*k3*k4 + k4^2)^(1/2) + 2))/(k2 - 2*L1 + k3 + k4 -
(2*k2*k3 - 2*k2*k4 + 2*k3*k4 + k2^2 + k3^2 + k4^2)^(1/2))^2 - (2*exp(L1*tau
- L1*t + (k2*t)/2 + (k3*t)/2 + (k4*t)/2 - (t*(k2^2 + 2*k2*k3 - 2*k2*k4 +
k3^2 + 2*k3*k4 + k4^2)^(1/2)))/2)*(2*L1*t - k2*t - k3*t - k4*t + t*(k2^2 +
2*k2*k3 - 2*k2*k4 + k3^2 + 2*k3*k4 + k4^2)^(1/2) + 2))/(k2 - 2*L1 + k3 + k4
- (2*k2*k3 - 2*k2*k4 + 2*k3*k4 + k2^2 + k3^2 + k4^2)^(1/2))^2) +
(2*A2*(exp((k2*tau)/2 + (k3*tau)/2 + (k4*tau)/2 - (tau*(k2^2 + 2*k2*k3 -
2*k2*k4 + k3^2 + 2*k3*k4 + k4^2)^(1/2)))/2) - exp(L1*tau - L1*t + (k2*t)/2 +
(k3*t)/2 + (k4*t)/2 - (t*(k2^2 + 2*k2*k3 - 2*k2*k4 + k3^2 + 2*k3*k4 +
k4^2)^(1/2)))/2)))/(k2 - 2*L1 + k3 + k4 - (k2^2 + 2*k2*k3 - 2*k2*k4 + k3^2 +
2*k3*k4 + k4^2)^(1/2)) + (2*A3*(exp((k2*tau)/2 + (k3*tau)/2 + (k4*tau)/2 -
(tau*(k2^2 + 2*k2*k3 - 2*k2*k4 + k3^2 + 2*k3*k4 + k4^2)^(1/2)))/2) -
exp(L1*tau - L1*t + (k2*t)/2 + (k3*t)/2 + (k4*t)/2 - (t*(k2^2 + 2*k2*k3 -
2*k2*k4 + k3^2 + 2*k3*k4 + k4^2)^(1/2)))/2)))/(k2 - 2*L1 + k3 + k4 - (k2^2 +
2*k2*k3 - 2*k2*k4 + k3^2 + 2*k3*k4 + k4^2)^(1/2)) - (2*A2*(exp((k2*tau)/2 +
(k3*tau)/2 + (k4*tau)/2 - (tau*(k2^2 + 2*k2*k3 - 2*k2*k4 + k3^2 + 2*k3*k4 +
k4^2)^(1/2)))/2) - exp(L2*tau - L2*t + (k2*t)/2 + (k3*t)/2 + (k4*t)/2 -
(t*(k2^2 + 2*k2*k3 - 2*k2*k4 + k3^2 + 2*k3*k4 + k4^2)^(1/2)))/2)))/(k2 -
2*L2 + k3 + k4 - (k2^2 + 2*k2*k3 - 2*k2*k4 + k3^2 + 2*k3*k4 + k4^2)^(1/2))
- (2*A3*(exp((k2*tau)/2 + (k3*tau)/2 + (k4*tau)/2 - (tau*(k2^2 + 2*k2*k3 -
2*k2*k4 + k3^2 + 2*k3*k4 + k4^2)^(1/2)))/2) - exp(L3*tau - L3*t + (k2*t)/2 +
(k3*t)/2 + (k4*t)/2 - (t*(k2^2 + 2*k2*k3 - 2*k2*k4 + k3^2 + 2*k3*k4 +
k4^2)^(1/2)))/2)))/(k2 - 2*L3 + k3 + k4 - (k2^2 + 2*k2*k3 - 2*k2*k4 + k3^2 +
2*k3*k4 + k4^2)^(1/2)) + (2*A1*tau*(exp((k2*tau)/2 + (k3*tau)/2 +
(k4*tau)/2 - (tau*(k2^2 + 2*k2*k3 - 2*k2*k4 + k3^2 + 2*k3*k4 +
k4^2)^(1/2)))/2) - exp(L1*tau - L1*t + (k2*t)/2 + (k3*t)/2 + (k4*t)/2 -
(t*(k2^2 + 2*k2*k3 - 2*k2*k4 + k3^2 + 2*k3*k4 + k4^2)^(1/2)))/2)))/(k2 -
2*L1 + k3 + k4 - (k2^2 + 2*k2*k3 - 2*k2*k4 + k3^2 + 2*k3*k4 + k4^2)^(1/2)))
```

```
+ k1*k3*exp(-(t*(k2 + k3 + k4 + (k2^2 + 2*k2*k3 - 2*k2*k4 + k3^2 + 2*k3*k4
+  k4^2)^(1/2)))/2)*(A1*((2*exp((k2*tau)/2  +  (k3*tau)/2  +  (k4*tau)/2  +
(tau*(k2^2 + 2*k2*k3 - 2*k2*k4 + k3^2 + 2*k3*k4 + k4^2)^(1/2))/2)*(k2*tau -
2*L1*tau + k3*tau + k4*tau + tau*(k2^2 + 2*k2*k3 - 2*k2*k4 + k3^2 + 2*k3*k4
+ k4^2)^(1/2) - 2))/(k2 - 2*L1 + k3 + k4 + (2*k2*k3 - 2*k2*k4 + 2*k3*k4 +
k2^2 + k3^2 + k4^2)^(1/2))^2 - (2*exp(L1*tau - L1*t + (k2*t)/2 + (k3*t)/2 +
(k4*t)/2  +  (t*(k2^2  +  2*k2*k3  -  2*k2*k4  +  k3^2  +  2*k3*k4  +
k4^2)^(1/2))/2)*(k2*t - 2*L1*t + k3*t + k4*t + t*(k2^2 + 2*k2*k3 - 2*k2*k4
+ k3^2 + 2*k3*k4 + k4^2)^(1/2) - 2))/(k2 - 2*L1 + k3 + k4 + (2*k2*k3 -
2*k2*k4 + 2*k3*k4 + k2^2 + k3^2 + k4^2)^(1/2))^2) +(2*A2*(exp(L1*tau - L1*t
+ (k2*t)/2 + (k3*t)/2 + (k4*t)/2 + (t*(k2^2 + 2*k2*k3 - 2*k2*k4 + k3^2 +
2*k3*k4  +  k4^2)^(1/2))/2)  -  exp((k2*tau)/2  +  (k3*tau)/2  +  (k4*tau)/2  +
(tau*(k2^2 + 2*k2*k3 - 2*k2*k4 + k3^2 + 2*k3*k4 + k4^2)^(1/2))/2)))/(k2 -
2*L1 + k3 + k4 + (k2^2 + 2*k2*k3 - 2*k2*k4 + k3^2 + 2*k3*k4 + k4^2)^(1/2))
+(2*A3*(exp(L1*tau - L1*t + (k2*t)/2 + (k3*t)/2 + (k4*t)/2 + (t*(k2^2 +
2*k2*k3 - 2*k2*k4 + k3^2 + 2*k3*k4 + k4^2)^(1/2))/2) - exp((k2*tau)/2 +
(k3*tau)/2 + (k4*tau)/2 + (tau*(k2^2 + 2*k2*k3 - 2*k2*k4 + k3^2 + 2*k3*k4 +
k4^2)^(1/2))/2)))/(k2 - 2*L1 + k3 + k4 + (k2^2 + 2*k2*k3 - 2*k2*k4 + k3^2 +
2*k3*k4 + k4^2)^(1/2)) -(2*A2*(exp(L2*tau - L2*t + (k2*t)/2 + (k3*t)/2 +
(k4*t)/2 + (t*(k2^2 + 2*k2*k3 - 2*k2*k4 + k3^2 + 2*k3*k4 + k4^2)^(1/2))/2)
- exp((k2*tau)/2 + (k3*tau)/2 + (k4*tau)/2 + (tau*(k2^2 + 2*k2*k3 - 2*k2*k4
+ k3^2 + 2*k3*k4 + k4^2)^(1/2))/2)))/(k2 - 2*L2 + k3 + k4 + (k2^2 + 2*k2*k3
-  2*k2*k4  +  k3^2  +  2*k3*k4  +  k4^2)^(1/2))  -(2*A3*(exp(L3*tau  -  L3*t  +
(k2*t)/2 + (k3*t)/2 + (k4*t)/2 + (t*(k2^2 + 2*k2*k3 - 2*k2*k4 + k3^2 +
2*k3*k4  +  k4^2)^(1/2))/2)  -  exp((k2*tau)/2  +  (k3*tau)/2  +  (k4*tau)/2  +
(tau*(k2^2 + 2*k2*k3 - 2*k2*k4 + k3^2 + 2*k3*k4 + k4^2)^(1/2))/2)))/(k2 -
2*L3 + k3 + k4 + (k2^2 + 2*k2*k3 - 2*k2*k4 + k3^2 + 2*k3*k4 + k4^2)^(1/2))
+(2*A1*tau*(exp(L1*tau - L1*t + (k2*t)/2 + (k3*t)/2 + (k4*t)/2 + (t*(k2^2 +
2*k2*k3 - 2*k2*k4 + k3^2 + 2*k3*k4 + k4^2)^(1/2))/2) - exp((k2*tau)/2 +
(k3*tau)/2 + (k4*tau)/2 + (tau*(k2^2 + 2*k2*k3 - 2*k2*k4 + k3^2 + 2*k3*k4 +
k4^2)^(1/2))/2)))/(k2 - 2*L1 + k3 + k4 + (k2^2 + 2*k2*k3 - 2*k2*k4 + k3^2 +
2*k3*k4  +  k4^2)^(1/2))))/(2*k2*k3  -  2*k2*k4  +  2*k3*k4  +  k2^2  +  k3^2  +
k4^2)^(1/2))
```

$c_{free}(t)$ =

```
(-(k1*exp(-(t*(k2 + k3 + k4 - (k2^2 + 2*k2*k3 - 2*k2*k4 + k3^2 +
2*k3*k4 + k4^2)^(1/2)))/2)*(k2 + k3 - k4 - (k2^2 + 2*k2*k3 - 2*k2*k4 + k3^2
+ 2*k3*k4 + k4^2)^(1/2))*(A1*((2*exp((k2*tau)/2 + (k3*tau)/2 + (k4*tau)/2 -
(tau*(k2^2 + 2*k2*k3 - 2*k2*k4 + k3^2 + 2*k3*k4 + k4^2)^(1/2))/2)*(2*L1*tau
- k2*tau - k3*tau - k4*tau + tau*(k2^2 + 2*k2*k3 - 2*k2*k4 + k3^2 + 2*k3*k4
+ k4^2)^(1/2) + 2))/(k2 - 2*L1 + k3 + k4 - (2*k2*k3 - 2*k2*k4 + 2*k3*k4 +
k2^2 + k3^2 + k4^2)^(1/2))^2 - (2*exp(L1*tau - L1*t + (k2*t)/2 + (k3*t)/2 +
(k4*t)/2  -  (t*(k2^2  +  2*k2*k3  -  2*k2*k4  +  k3^2  +  2*k3*k4  +
k4^2)^(1/2))/2)*(2*L1*t - k2*t - k3*t - k4*t + t*(k2^2 + 2*k2*k3 - 2*k2*k4
+ k3^2 + 2*k3*k4 + k4^2)^(1/2) + 2))/(k2 - 2*L1 + k3 + k4 - (2*k2*k3 -
2*k2*k4 + 2*k3*k4 + k2^2 + k3^2 + k4^2)^(1/2))^2) + (2*A2*(exp((k2*tau)/2 +
(k3*tau)/2 + (k4*tau)/2 - (tau*(k2^2 + 2*k2*k3 - 2*k2*k4 + k3^2 + 2*k3*k4 +
k4^2)^(1/2))/2) - exp(L1*tau - L1*t + (k2*t)/2 + (k3*t)/2 + (k4*t)/2 -
(t*(k2^2 + 2*k2*k3 - 2*k2*k4 + k3^2 + 2*k3*k4 + k4^2)^(1/2))/2)))/(k2 -
2*L1 + k3 + k4 - (k2^2 + 2*k2*k3 - 2*k2*k4 + k3^2 + 2*k3*k4 + k4^2)^(1/2))
+ (2*A3*(exp((k2*tau)/2 + (k3*tau)/2 + (k4*tau)/2 - (tau*(k2^2 + 2*k2*k3 -
2*k2*k4 + k3^2 + 2*k3*k4 + k4^2)^(1/2))/2) - exp(L1*tau - L1*t + (k2*t)/2 +
(k3*t)/2 + (k4*t)/2 - (t*(k2^2 + 2*k2*k3 - 2*k2*k4 + k3^2 + 2*k3*k4 +
k4^2)^(1/2))/2)))/(k2 - 2*L1 + k3 + k4 - (k2^2 + 2*k2*k3 - 2*k2*k4 + k3^2 +
2*k3*k4 + k4^2)^(1/2)) - (2*A2*(exp((k2*tau)/2 + (k3*tau)/2 + (k4*tau)/2 -
```

```
(tau*(k2^2 + 2*k2*k3 - 2*k2*k4 + k3^2 + 2*k3*k4 + k4^2)^(1/2))/2) -
exp(L2*tau - L2*t + (k2*t)/2 + (k3*t)/2 + (k4*t)/2 - (t*(k2^2 + 2*k2*k3 -
2*k2*k4 + k3^2 + 2*k3*k4 + k4^2)^(1/2))/2)))/(k2 - 2*L2 + k3 + k4 - (k2^2 +
2*k2*k3 - 2*k2*k4 + k3^2 + 2*k3*k4 + k4^2)^(1/2)) - (2*A3*(exp((k2*tau)/2 +
(k3*tau)/2 + (k4*tau)/2 - (tau*(k2^2 + 2*k2*k3 - 2*k2*k4 + k3^2 + 2*k3*k4 +
k4^2)^(1/2))/2) - exp(L3*tau - L3*t + (k2*t)/2 + (k3*t)/2 + (k4*t)/2 -
(t*(k2^2 + 2*k2*k3 - 2*k2*k4 + k3^2 + 2*k3*k4 + k4^2)^(1/2))/2)))/(k2 -
2*L3 + k3 + k4 - (k2^2 + 2*k2*k3 - 2*k2*k4 + k3^2 + 2*k3*k4 + k4^2)^(1/2))
+ (2*A1*tau*(exp((k2*tau)/2 + (k3*tau)/2 + (k4*tau)/2 - (tau*(k2^2 +
2*k2*k3 - 2*k2*k4 + k3^2 + 2*k3*k4 + k4^2)^(1/2))/2) - exp(L1*tau - L1*t +
(k2*t)/2 + (k3*t)/2 + (k4*t)/2 - (t*(k2^2 + 2*k2*k3 - 2*k2*k4 + k3^2 +
2*k3*k4 + k4^2)^(1/2))/2)))/(k2 - 2*L1 + k3 + k4 - (k2^2 + 2*k2*k3 -
2*k2*k4 + k3^2 + 2*k3*k4 + k4^2)^(1/2))))/(2*(2*k2*k3 - 2*k2*k4 + 2*k3*k4 +
k2^2 + k3^2 + k4^2)^(1/2)) - (k1*exp(-(t*(k2 + k3 + k4 + (k2^2 + 2*k2*k3 -
2*k2*k4 + k3^2 + 2*k3*k4 + k4^2)^(1/2)))/2)*(k2 + k3 - k4 + (k2^2 + 2*k2*k3
- 2*k2*k4 + k3^2 + 2*k3*k4 + k4^2)^(1/2))*(A1*((2*exp((k2*tau)/2 +
(k3*tau)/2 + (k4*tau)/2 + (tau*(k2^2 + 2*k2*k3 - 2*k2*k4 + k3^2 + 2*k3*k4 +
k4^2)^(1/2))/2)*(k2*tau - 2*L1*tau + k3*tau + k4*tau + tau*(k2^2 + 2*k2*k3
- 2*k2*k4 + k3^2 + 2*k3*k4 + k4^2)^(1/2) - 2))/(k2 - 2*L1 + k3 + k4 +
(2*k2*k3 - 2*k2*k4 + 2*k3*k4 + k2^2 + k3^2 + k4^2)^(1/2))^2 - (2*exp(L1*tau
- L1*t + (k2*t)/2 + (k3*t)/2 + (k4*t)/2 + (t*(k2^2 + 2*k2*k3 - 2*k2*k4 +
k3^2 + 2*k3*k4 + k4^2)^(1/2))/2)*(k2*t - 2*L1*t + k3*t + k4*t + t*(k2^2 +
2*k2*k3 - 2*k2*k4 + k3^2 + 2*k3*k4 + k4^2)^(1/2) - 2))/(k2 - 2*L1 + k3 + k4
+ (2*k2*k3 - 2*k2*k4 + 2*k3*k4 + k2^2 + k3^2 + k4^2)^(1/2))^2) +
(2*A2*(exp(L1*tau - L1*t + (k2*t)/2 + (k3*t)/2 + (k4*t)/2 + (t*(k2^2 +
2*k2*k3 - 2*k2*k4 + k3^2 + 2*k3*k4 + k4^2)^(1/2))/2) - exp((k2*tau)/2 +
(k3*tau)/2 + (k4*tau)/2 + (tau*(k2^2 + 2*k2*k3 - 2*k2*k4 + k3^2 + 2*k3*k4 +
k4^2)^(1/2))/2)))/(k2 - 2*L1 + k3 + k4 + (k2^2 + 2*k2*k3 - 2*k2*k4 + k3^2 +
2*k3*k4 + k4^2)^(1/2)) + (2*A3*(exp(L1*tau - L1*t + (k2*t)/2 + (k3*t)/2 +
(k4*t)/2 + (t*(k2^2 + 2*k2*k3 - 2*k2*k4 + k3^2 + 2*k3*k4 + k4^2)^(1/2))/2)
- exp((k2*tau)/2 + (k3*tau)/2 + (k4*tau)/2 + (tau*(k2^2 + 2*k2*k3 - 2*k2*k4
+ k3^2 + 2*k3*k4 + k4^2)^(1/2))/2)))/(k2 - 2*L1 + k3 + k4 + (k2^2 + 2*k2*k3
- 2*k2*k4 + k3^2 + 2*k3*k4 + k4^2)^(1/2)) - (2*A2*(exp(L2*tau - L2*t +
(k2*t)/2 + (k3*t)/2 + (k4*t)/2 + (t*(k2^2 + 2*k2*k3 - 2*k2*k4 + k3^2 +
2*k3*k4 + k4^2)^(1/2))/2) - exp((k2*tau)/2 + (k3*tau)/2 + (k4*tau)/2 +
(tau*(k2^2 + 2*k2*k3 - 2*k2*k4 + k3^2 + 2*k3*k4 + k4^2)^(1/2))/2)))/(k2 -
2*L2 + k3 + k4 + (k2^2 + 2*k2*k3 - 2*k2*k4 + k3^2 + 2*k3*k4 + k4^2)^(1/2))
- (2*A3*(exp(L3*tau - L3*t + (k2*t)/2 + (k3*t)/2 + (k4*t)/2 + (t*(k2^2 +
2*k2*k3 - 2*k2*k4 + k3^2 + 2*k3*k4 + k4^2)^(1/2))/2) - exp((k2*tau)/2 +
(k3*tau)/2 + (k4*tau)/2 + (tau*(k2^2 + 2*k2*k3 - 2*k2*k4 + k3^2 + 2*k3*k4 +
k4^2)^(1/2))/2)))/(k2 - 2*L3 + k3 + k4 + (k2^2 + 2*k2*k3 - 2*k2*k4 + k3^2 +
2*k3*k4 + k4^2)^(1/2)) + (2*A1*tau*(exp(L1*tau - L1*t + (k2*t)/2 + (k3*t)/2
+ (k4*t)/2 + (t*(k2^2 + 2*k2*k3 - 2*k2*k4 + k3^2 + 2*k3*k4 +
k4^2)^(1/2))/2) - exp((k2*tau)/2 + (k3*tau)/2 + (k4*tau)/2 + (tau*(k2^2 +
2*k2*k3 - 2*k2*k4 + k3^2 + 2*k3*k4 + k4^2)^(1/2))/2)))/(k2 - 2*L1 + k3 + k4
+ (k2^2 + 2*k2*k3 - 2*k2*k4 + k3^2 + 2*k3*k4 + k4^2)^(1/2))))/(2*(2*k2*k3 -
2*k2*k4 + 2*k3*k4 + k2^2 + k3^2 + k4^2)^(1/2)))
```

APPENDIX C : Monte Carlo Method and GATE

The Monte Carlo method is an effective way to simulate complex models using a statistical instead of a analytical approach. Despite its long computation times, the Monte Carlo method offers a good approximation of the true solution and is therefore ideal for simulation of nuclear imaging. By iteratively evaluating a deterministic model using a large number of random inputs, systems with a many degrees of freedom can be estimated, where the accuracy increases with the amount of samples. Many packages and algorithms are available for different systems and physical processes, ranging from fluid dynamics to nuclear physics. The main advantage of using Monte Carlo estimations is that one has complete control over the input of the system.

For this particular project, the GATE package was used. GATE is a Monte Carlo package specifically for nuclear imaging and radiotherapy and is built on the widely used Geant4 simulation toolkit by CERN. The first version of GATE was released in 2004 and is since then used in a large number of papers, including some for the Siemens Biograph.

References

[1] K. Chen, D. Bandy, E. Reiman, S. C. Huang, M. Lawson, D. Feng, L. S. Yun, and A. Palant, "Noninvasive quantification of the cerebral metabolic rate for glucose using positron emission tomography, 18F-fluoro-2-deoxyglucose, the Patlak method, and an image-derived input function.," *J. Cereb. blood flow Metab.*, vol. 18, no. 7, pp. 716–23, Jul. 1998.

[2] J. E. M. Mourik, M. Lubberink, U. M. H. Klumpers, E. F. Comans, A. a Lammertsma, and R. Boellaard, "Partial volume corrected image derived input functions for dynamic PET brain studies: methodology and validation for [11C]flumazenil.," *Neuroimage*, vol. 39, no. 3, pp. 1041–50, Feb. 2008.

[3] S. Hackett and D. Liu, "Estimation of input functions from dynamic FLT PET studies of the head and neck with correction for partial volume effects," *Eur. J. Nucl. Med. …*, pp. 1–9, 2013.

[4] B. W. Jakoby, Y. Bercier, M. Conti, M. E. Casey, B. Bendriem, and D. W. Townsend, "Physical and clinical performance of the mCT time-of-flight PET/CT scanner.," *Phys. Med. Biol.*, vol. 56, no. 8, pp. 2375–89, Apr. 2011.

[5] I. Bakker, "Prostaatkanker syllabus," 2013.

[6] I. Bakker, "Clinical trial with Sarabesin 3 , a GRP receptor antagonist , labelled with gallium-68 , in patients with prostate cancer confined to the primary organ," 2014.

[7] R. Boellaard, M. J. O'Doherty, W. a. Weber, F. M. Mottaghy, M. N. Lonsdale, S. G. Stroobants, W. J. G. Oyen, J. Kotzerke, O. S. Hoekstra, J. Pruim, P. K. Marsden, K. Tatsch, C. J. Hoekstra, E. P. Visser, B. Arends, F. J. Verzijlbergen, J. M. Zijlstra, E. F. I. Comans, A. a. Lammertsma, A. M. Paans, A. T. Willemsen, T. Beyer, A. Bockisch, C. Schaefer-Prokop, D. Delbeke, R. P. Baum, A. Chiti, and B. J. Krause, "FDG PET and PET/CT: EANM procedure guidelines for tumour PET imaging: Version 1.0," *Eur. J. Nucl. Med. Mol. Imaging*, vol. 37, no. 1, pp. 181–200, 2010.

[8] H. Gavin, "The Levenberg-Marquardt method for nonlinear least squares curve-fitting problems," *Dep. Civ. Environ. Eng. …*, pp. 1–17, 2011.

[9] R. P. Maguire and K. L. Leenders, "Course Manual PET Pharmacokinetic International Society of Cerebral Blood Flow and Metabolism Summerschool 2007," *J. Cereb. blood flow Metab.*, 2007.

[10] I. Velikyan, A. Sundin, J. Sörensen, M. Lubberink, M. Sandström, U. Garske-Román, H. Lundqvist, D. Granberg, and B. Eriksson, "Quantitative and qualitative intrapatient comparison of 68Ga-DOTATOC and 68Ga-DOTATATE: net uptake rate for accurate quantification.," *J. Nucl. Med.*, vol. 55, no. 2, pp. 204–10, Feb. 2014.

[11] P. J. Green, "Iteratively Reweighted Least Squares for Maximum Likelihood Estimation , and some Robust and Resistant Alternatives," *J. R. Stat. Soc.*, vol. 46, no. 2, pp. 149–192, 1987.

[12] L. YC, C. TH, C. CY, N. SH, L. HL, W. KC, W. YY, W. CC, and W. JJ., "Blind estimation of the arterial input function in dynamic contrast-enhanced MRI using purity maximization.," *Magn. Reson. Med.*, vol. 68, no. 5, pp. 1439–49, 2012.

[13] P. Millet, J. Delforge, S. Pappata, L. Cinotti, V. Frouin, Y. Samson, and B. Bendriem, "Parameter and Index Images of Benzodiazepine Receptor Concentration in the Brain," *J. Nucl. Med.*, vol. 36, no. 8, pp. 1462–1471, 1995.

[14] L. Bouchet and W. Bolch, "MIRD Pamphlet No. 19: Absorbed fractions and radionuclide S values for six age-dependent multiregion models of the kidney," *J. Nucl. …*, vol. 7, no. 19, pp. 1113–1147, 2003.

[15] A. J. J. Bos, F. S. Draaisma, and W. J. C. Okx, *Inleiding tot de stralingshygiëne*. 2007.

[16] M. G. Stabin, R. B. Sparks, and E. Crowe, "OLINDA/EXM: the second-generation personal computer software for internal dose assessment in nuclear medicine.," *J. Nucl. Med.*, vol. 46, no. 6, pp. 1023–1027, 2005.

[17] F. Forrer, E. P. Krenning, P. P. Kooij, B. F. Bernard, M. Konijnenberg, W. H. Bakker, J. J. M. Teunissen, M. De Jong, K. Van Lom, W. W. De Herder, and D. J. Kwekkeboom, "Bone marrow dosimetry in peptide receptor radionuclide therapy with [177Lu-DOTA0,Tyr3]octreotate," *Eur. J. Nucl. Med. Mol. Imaging*, vol. 36, no. 7, pp. 1138–1146, 2009.

[18] S. Jan, G. Santin, D. Strul, S. Staelens, K. Assié, D. Autret, S. Avner, R. Barbier, M. Bardiès, P. M. Bloomfield, D. Brasse, V. Breton, P. Bruyndonckx, I. Buvat, a F. Chatziioannou, Y. Choi, Y. H. Chung, C. Comtat, D. Donnarieix, L. Ferrer, S. J. Glick, C. J. Groiselle, D. Guez, P. F. Honore, S. Kerhoas-Cavata, a S. Kirov, V. Kohli, M. Koole, M. Krieguer, D. J. van der Laan, F. Lamare, G. Largeron, C. Lartizien, D. Lazaro, M. C. Maas, L. Maigne, F. Mayet, F. Melot, C. Merheb, E. Pennacchio, J. Perez, U. Pietrzyk, F. R. Rannou, M. Rey, D. R. Schaart, C. R. Schmidtlein, L. Simon, T. Y. Song, J. M. Vieira, D. Visvikis, R. Van de Walle, E. Wieërs, and C. Morel, "GATE: a simulation toolkit for PET and SPECT.," *Phys. Med. Biol.*, vol. 49, no. 19, pp. 4543–4561, 2004.

[19] P. Gonias, N. Bertsekas, N. Karakatsanis, G. Saatsakis, a. Gaitanis, D. Nikolopoulos, G. Loudos, L. Papaspyrou, N. Sakellios, X. Tsantilas, a. Daskalakis, P. Liaparinos, K. Nikita, a. Louizi, D. Cavouras, I. Kandarakis, and G. S. Panayiotakis, "Validation of a GATE model for the simulation of the Siemens biograph™ 6 PET scanner," *Nucl. Instruments Methods Phys. Res. Sect. A Accel. Spectrometers, Detect. Assoc. Equip.*, vol. 571, no. 1–2 SPEC. ISS., pp. 263–266, 2007.

[20] S. Camarasu-Pop, T. Glatard, R. F. Da Silva, P. Gueth, D. Sarrut, and H. Benoit-Cattin, "Monte Carlo simulation on heterogeneous distributed systems: A computing framework with parallel merging and checkpointing strategies," *Futur. Gener. Comput. Syst.*, vol. 29, no. 3, pp. 728–738, 2013.

[21] J. K. Poon, M. L. Dahlbom, W. W. Moses, K. Balakrishnan, S. R. Cherry, and R. D. Badawi, "volumes of LSO scintillator : a simulation study," vol. 57, no. 13, pp. 4077–4094, 2013.

[22] J. Prince and J. Links, *Medical Imaging Signals & Systems*. 2005.

[23] B. W. Jakoby, Y. Bercier, M. Conti, M. E. Casey, B. Bendriem, and D. W. Townsend, "Physical and clinical performance of the mCT time-of-flight PET/CT scanner.," *Phys. Med. Biol.*, vol. 56, no. 8, pp. 2375–89, Apr. 2011.

[24] S. St James and C. Thompson, "Image blurring due to light-sharing in PET block detectors.," *Med. Phys.*, vol. 33, no. 2, pp. 405–410, 2006.

[25] T. Inaba, “Quantitative measurements of prostatic blood flow and blood volume by positron emission tomography.,” *J. Urol.*, vol. 148, no. 5, pp. 1457–1460, 1992.

[26] E. Marieb and K. Hoehn, *Human Anatomy & Physiology*. 2013.

[27] ICRP, “Radiation Dose to Patients from Radiopharmaceuticals - Addendum 3 to ICRP Publication 53,” 2008.

[28] K. Herrmann, C. Lapa, H. Wester, M. Schottelius, C. Schiepers, U. Eberlein, C. Bluemel, U. Keller, A. Knop, S. Kropf, A. Schirbel, A. Buck, and M. Lassmann, “Biodistribution and radiation dosimetry for the chemokine receptor CXCR4-targeting probe 68Ga-pentixafor.,” *J. Nucl. Med.*, vol. 56, no. 3, pp. 410–416, 2015.

[29] M. Sandström, I. Velikyan, U. Garske-Román, J. Sörensen, B. Eriksson, D. Granberg, H. Lundqvist, A. Sundin, and M. Lubberink, “Comparative biodistribution and radiation dosimetry of 68Ga-DOTATOC and 68Ga-DOTATATE in patients with neuroendocrine tumors.,” *J. Nucl. Med.*, vol. 54, no. 10, pp. 1755–9, 2013.

[30] K. Herrmann, C. Bluemel, M. Weineisen, M. Schottelius, H.-J. Wester, J. Czernin, U. Eberlein, S. Beykan, C. Lapa, H. Riedmiller, M. Krebs, S. Kropf, a. Schirbel, a. K. Buck, and M. Lassmann, “Biodistribution and radiation dosimetry for a novel probe targeting prostate specific membrane antigen for Imaging and Therapy (68Ga-PSMA I&T),” *J. Nucl. Med.*, pp. 855–862, 2015.

[31] H. W. Watabe, Y. I. Koma, Y. K. Imura, M. N. Aganawa, and M. S. Hidahara, “PET kinetic analysis — compartmental model,” *Ann. Nucl. Med.*, vol. 20, no. 9, pp. 583–588, 2006.

[32] B. J. Beattie, P. M. Smith-Jones, Y. S. Jhanwar, H. Schöder, C. R. Schmidtlein, M. J. Morris, P. Zanzonico, O. Squire, G. S. P. Meirelles, R. Finn, M. Namavari, S. Cai, H. I. Scher, S. M. Larson, and J. L. Humm, “Pharmacokinetic assessment of the uptake of 16beta-18F-fluoro-5alpha-dihydrotestosterone (FDHT) in prostate tumors as measured by PET.,” *J. Nucl. Med.*, vol. 51, no. 2, pp. 183–92, Feb. 2010.

[33] M. a Kropholler, R. Boellaard, A. Schuitemaker, B. N. M. van Berckel, G. Luurtsema, A. D. Windhorst, and A. a Lammertsma, “Development of a tracer kinetic plasma input model for (R)-[11C]PK11195 brain studies.,” *J. Cereb. blood flow Metab.*, vol. 25, no. 7, pp. 842–51, Jul. 2005.